

# Cluster-Based Approach Utilizing Optimally Tuned TD-DFT to Calculate Absorption Spectra of Organic Semiconductor Thin Films

Published as part of Journal of Chemical Theory and Computation *virtual special issue* "First-Principles Simulations of Molecular Optoelectronic Materials: Elementary Excitations and Spatiotemporal Dynamics".

Luca Craciunescu, Maximilian Asbach, Sara Wirsing, Sebastian Hammer, Frederik Unger, Katharina Broch, Frank Schreiber, Gregor Witte, Andreas Dreuw, Petra Tegeder, Felipe Fantuzzi, and Bernd Engels\*



Cite This: *J. Chem. Theory Comput.* 2023, 19, 9369–9387



Read Online

ACCESS |



Metrics & More

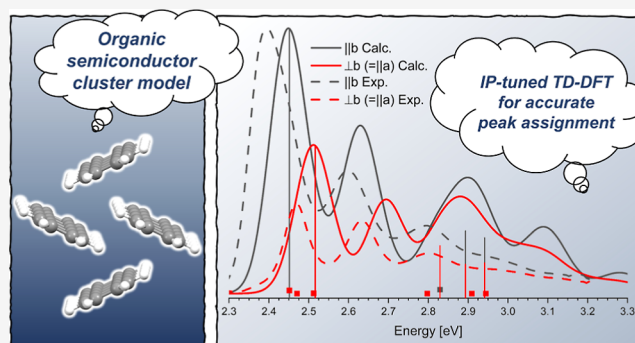


Article Recommendations



Supporting Information

**ABSTRACT:** The photophysics of organic semiconductor (OSC) thin films or crystals has garnered significant attention in recent years since a comprehensive theoretical understanding of the various processes occurring upon photoexcitation is crucial for assessing the efficiency of OSC materials. To date, research in this area has relied on methods using Frenkel–Holstein Hamiltonians, calculations of the GW–Bethe–Salpeter equation with periodic boundaries, or cluster-based approaches using quantum chemical methods, with each of the three approaches having distinct advantages and disadvantages. In this work, we introduce an optimally tuned, range-separated time-dependent density functional theory approach to accurately reproduce the total and polarization-resolved absorption spectra of pentacene, tetracene, and perylene thin films, all representative OSC materials. Our approach achieves excellent agreement with experimental data (mostly  $\leq 0.1$  eV) when combined with the utilization of clusters comprising multiple monomers and a standard polarizable continuum model to simulate the thin-film environment. Our protocol therefore addresses a major drawback of cluster-based approaches and makes them attractive tools for OSC investigations. Its key advantages include its independence from external, system-specific fitting parameters and its straightforward application with well-known quantum chemical program codes. It demonstrates how chemical intuition can help to reduce computational cost and still arrive at chemically meaningful and almost quantitative results.



## 1. INTRODUCTION

Organic semiconductors (OSCs) have been intensively investigated for many years, as their structural flexibility, chemical tunability, and low production costs would be ideal prerequisites for efficient electronic devices. While in the field of light-emitting diodes, market readiness has already been achieved, in other areas, the efficiency still has to be significantly increased. For the development of efficient design and optimization strategies for new materials, suitable theoretical approaches are needed, but they pose fundamental challenges. These arise from the fact that most material properties are determined by a large number of competing processes and a complicated interplay between the molecular units. The resulting size of the system combined with the complexity of the electronic structure of aggregates of organic semiconductors makes reliable calculations very challenging.

Three main approaches have emerged for describing OSCs, each with its advantages and disadvantages. A very important and very successful approach is based on model Hamiltonians,

such as the Holstein–Peierls approach.<sup>1,2</sup> Such approaches can handle very large systems and therefore provide very detailed assignments of spectra.<sup>3–5</sup> Newer approaches can also accurately describe the formation of excimers.<sup>6</sup> Nevertheless, problems arise in the prediction of new materials since many of the necessary parameters rely on available experimental data.

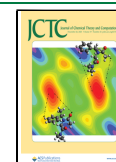
Solid-state approaches involving the Bethe–Salpeter equation (BSE) in combination with the GW approximation provide very accurate information about the total and even polarization-resolved absorption spectra of crystals or different polymorphs of thin films. Further advantages arise because these approaches formally consider the entire crystal or thin

Received: October 6, 2023

Revised: November 24, 2023

Accepted: November 27, 2023

Published: December 11, 2023



film.<sup>7–12</sup> However, the required periodic boundary conditions complicate the description of local disorder or relaxation effects such as the formation of excimers.

Cluster approaches considering only a small region of the total system have exactly opposite problems. Local perturbations or relaxation processes like excimer formation can apparently be described very well, as many successful studies indicate.<sup>13–19</sup> On the other hand, for effects that are essentially based on delocalized excitons, such as absorption spectra, such approaches fail. This failure naturally raises the question of whether the agreement with experimental data found in the description of relaxation processes is due to fortuitous error compensation.

In a recent study,<sup>20</sup> we showed that the erroneous description of the absorption spectrum of the pentacene crystal by cluster approaches using linear-response time-dependent density functional theory (TD-DFT) results from two major sources of error. First, the use of standard range-separated exchange–correlation (xc) functionals such as  $\omega$ B97X-D3 does not capture the energy position of charge-transfer states with sufficient accuracy. In addition, only those clusters in which the environment of the individual monomers is as similar as possible are suitable for description. Tiny differences in their environments already cause localization of excitons on individual monomers, resulting in incorrect spectra. In contrast, if suitable clusters are used and optimal tuning is applied to correct the range-separated functionals,<sup>21,22</sup> excellent accuracy is obtained for both the total and the polarization-resolved absorption spectra.

Beyond our previous proof of principle,<sup>20</sup> this paper gives a more detailed insight into our cluster-based approach, including dependencies on different factors such as the composition of the clusters and their geometries, the range-separation parameters, the choice of xc-functionals and basis sets. Additionally, the influence of vibrational effects is investigated. For further validations, calculations were carried out for tetracene analogous to those for pentacene. Both are prototypical OSCs for which countless experimental and theoretical studies investigating their thin films and crystals have been published.<sup>3–5,9,12,23–27</sup> A list of works and a short summary of the respective results are given in Tables S1 and S2. Finally, to demonstrate the transferability of our protocol to more complex crystal structures, we employed it to simulate the absorption spectrum of the monoclinic  $\alpha$ -phase of perylene.

To investigate the possible effects of error compensations, we have performed benchmark calculations. Multireference approaches like MR-CI or CASPT2 provide ideal reference results for benchmarks due to their ability to deliver very accurate results for excited states,<sup>28–31</sup> potential energy surfaces,<sup>32,33</sup> as well as other molecular properties.<sup>34–36</sup> With some limitations, this also applies to linear-response approaches such as CC2,<sup>37</sup> their spin-component scaling (SCS) variants,<sup>38,39</sup> and coupled-cluster approaches like DLPNO-STEOM-CCSD.<sup>40–42</sup> However, for systems with many atoms as the clusters investigated in this work, they are computationally too expensive. Hence, we tested the accuracy of TD-DFT calculations using pentacene and tetracene monomers as model systems.

This work is organized as follows: we commence by providing technical details and proceed to assess the accuracy of different quantum chemical approaches. This evaluation involves comparison with experimental data and highly

correlated wave function-based computations for single OSC molecules. Notably, we conduct these calculations for single molecules due to their computational cost, which becomes prohibitive when dealing with the molecular clusters used in subsequent analyses. We then explore the use of molecular clusters to simulate the absorption spectra of the OSC crystals, investigate photoinduced relaxation effects, and assess the influence of vibrations. Section 3.3 comprises the simulations of the total and polarization-resolved spectra, including peak assignments and comparisons with the previous results. Sections 3.4 and 3.5 are dedicated to discussing the criteria governing the selection of clusters, xc-functionals, and atomic basis sets to achieve good agreement with experimental measurements. Finally, in Section 3.6, we present our calculations for the spectra of  $\alpha$ -perylene crystals. There, we focus on electronic effects and the prerequisites for cluster selection. Finally, our work concludes with a summary of the main results and an outlook.

## 2. COMPUTATIONAL DETAILS

The Orca software package<sup>43–45</sup> was employed for TD-DFT calculations in both vacuum and utilizing the polarizable continuum model (PCM). In selected cases within the PCM approach, complementary calculations using the Q-Chem 5.3 software<sup>46</sup> were also performed. CASPT2 calculations were conducted using OpenMolcas,<sup>47,48</sup> where  $[x, y]$  indicates the active space comprising  $x$  electrons in  $y$  orbitals. State-averaged (SA) and state-specific (SS) calculations were performed. In some calculations, we introduced an imaginary shift in the perturbation theory correction, denoted as “Im.”, to avoid the problem of weak intruder states.<sup>49</sup> The resolution of identity (RI)<sup>50,51</sup> approximation and SCS<sup>38,39</sup> were applied for SCS-ADC(2) and SCS-CC2 calculations, which were done using Turbomole 7.4.<sup>52</sup> Excited state analyses were performed with TheoDORE 2.3.<sup>53</sup> In this case, we employed electron–hole correlation plots (e–h plots) to gain insights into the character of the various excitations with respect to selected fragments of the whole system. Diagonal positions indicate local excitations on a given fragment, often termed Frenkel excitations. Nondiagonal elements, on the other hand, represent excitations between fragments, often labeled as charge-transfer (CT) states. In these plots, the shading of the square corresponds to the proportion of this position to the excited state, with darker squares indicating a higher contribution. The CT value ranges from 0 to 1, where 0 stands for a pure Frenkel and 1 indicates a pure CT excitation. Another essential descriptor employed in our analysis is the participation ratio (PR), which quantifies the number of fragments involved in a given excited state. For tetracene and pentacene, each monomer served as a single fragment. However, for perylene, we selected dimers as the fundamental units (further details are provided below). Additionally, the RMSeh value denotes the mean distance between the electron and hole and is measured in Å.

The works of Spano and co-workers underscore the critical importance of correctly describing the mixing between Frenkel and CT states for accurate simulations of the absorption spectra of thin films of pentacene and tetracene.<sup>3,5</sup> For CT states, gradient-corrected or hybrid functionals often underestimate the excitation energies by more than 1 eV,<sup>54</sup> while TD-HF overestimates their excitation energies by 1 eV or more.<sup>55,56</sup> Range-separated functionals provide more accurate predictions for CT states<sup>57–59</sup> but still tend to overestimate

their excitation energies. Recently, it has been found that the so-called optimally tuned functionals give very accurate predictions, especially for CT states.<sup>21</sup> Optimally tuned functionals are range-separated functionals for which the corresponding range-separation parameter  $\omega$  is tuned by minimizing the following quantity<sup>60,61</sup>

$$J(\omega) = (\epsilon_{\text{HOMO}}(\omega) + \text{IP}(\omega))^2 + (\epsilon_{\text{LUMO}}(\omega) + \text{EA}(\omega))^2 \quad (1)$$

where IP is the computed ionization potential, EA the computed electron affinity, and  $\epsilon_{\text{HOMO}}$  and  $\epsilon_{\text{LUMO}}$  are the highest occupied molecular orbital (HOMO) and lowest unoccupied molecular orbital (LUMO) energies. The range-separation parameter  $\omega$  that minimizes eq 1 is then used in the subsequent TD-DFT computations. This procedure has the advantage that  $\omega$  is not fitted with respect to some experimental parameter but enforces Koopmans' theorem for the neutral and anionic systems as accurately as possible. Please note that Koopmans' theorem should hold for the exact Kohn–Sham theory.<sup>62,63</sup> Hence, a better description of CT states may occur since computed ionization energies are strongly improved in this approach.<sup>64</sup>

The exchange energy of a range-separated functional is given by the following components

$$E_{\text{xc}}^{\text{RSH}} = \alpha E_{\text{x,F}}^{\text{SR},\omega} + (1 - \alpha) E_{\text{x,GGA}}^{\text{SR},\omega} + (\alpha + \beta) E_{\text{x,F}}^{\text{LR},\omega} + (1 - \alpha - \beta) E_{\text{x,GGA}}^{\text{LR},\omega} + E_{\text{c,GGA}} \quad (2)$$

In vacuum,  $\alpha + \beta = 1$  for the potential to be asymptotically correct. For  $\omega\text{B97X-D3}$ ,  $\alpha = 0.2$ . If optimal tuning is performed in vacuum,  $\alpha$  and  $\beta$  are left unchanged, and only the parameter  $\omega$  appearing in  $E_{\text{x,GGA}}^{\text{SR},\omega}$ ,  $E_{\text{x,F}}^{\text{LR},\omega}$ , and  $E_{\text{x,GGA}}^{\text{LR},\omega}$  is varied. To distinguish between standard and optimally tuned functionals, the latter are marked with the subscript T (e.g.,  $\omega\text{T-B97X-D3}$  instead of  $\omega\text{B97X-D3}$ ). Unless otherwise noted, we employed this kind of optimal tuning in the present work. In the actual computation of the spectra, we used the resulting  $\omega$  value in combination with a conductor-like polarizable continuous model (C-PCM)<sup>65</sup> with  $\epsilon = 3$  and  $n = 1.7$  to account for polarization effects arising from the neglected crystal environment.

Besides the optimal tuning in vacuum, other approaches were suggested. In the dielectric screening approach as described by Kronik and Kümmel<sup>66</sup> and references therein, the dielectric constant  $\epsilon$  is incorporated directly into the functional by enforcing  $\alpha + \beta = 1/\epsilon$  to account for the environment. In our specific case with  $\epsilon = 3$  and  $\alpha = 0.2$ ,  $\beta$  was therefore changed to 0.133. However, this approach was found to be inappropriate for the investigated systems (see Supporting Information Section S12). Alternatively, the optimal tuning procedure can also be performed with PCM included, even though this approach is generally discouraged in the literature.<sup>66</sup> Nevertheless, we performed tests using this approach, but the results indicated its inappropriateness (see below).

Direct computations relying on simple crystal structure data are often susceptible to errors stemming from experimental factors, such as the position of hydrogen atoms or theoretical deficiencies. Performing full cluster geometry optimizations mostly yields inaccurate structures, as they do not consider the steric influence of the crystal environment. Therefore, we employed a two-step procedure to optimize both intra- and intermonomeric geometries. First, the cluster structures were

extracted from the respective crystal structures, obtained from Schiefer et al.<sup>67</sup> for pentacene and Campbell et al.<sup>68</sup> for tetracene. Fully optimized monomer structures, utilizing  $\omega\text{B97X-D3/def2-SVP}$  with cluster-specific  $\omega$  and PCM, were subsequently positioned at the center of mass of the molecules within the crystal structure unless explicitly stated otherwise. The influence of using optimized monomer structures is substantial, particularly on the total energy. When employing the experimental crystal structure without any optimization, the ground-state energy is approximately 18 eV higher than that of the structure where monomers were optimized. In contrast, optimizing only the C–H bonds results in a marginal energy increase of merely 0.11 eV.

To include broadening effects in the absorption spectra, the electronic stick spectra obtained from the transition dipole moment of the excitations ( $T^2$ ) were superimposed with Gaussian functions [full width at half-maximum of 100 meV]. Vibrational effects were explicitly included as described below.

### 3. RESULTS AND DISCUSSION

**3.1. Benchmark Calculations for the Pentacene Monomer.** Due to their molecular size, the employed clusters are too large to perform a benchmark against high-level wave function-based approaches. Thus, we rely on pentacene and tetracene monomers for this purpose, and their computed values in this study are presented in Tables 1 and S8, respectively. In turn, Tables 2 and S9 list selected previous computational and experimental results with which our data are compared. It is noteworthy that the often cited experimental 0–0 transition by Biermann and Schmidt<sup>69</sup> is, in fact, a theoretically corrected value extrapolated from solution spectra.

In our previous work,<sup>20</sup> we compared the accuracy of DFT and wave function-based methods for the  $S_1$  state of the pentacene monomer. In the present work, we extend the investigation to the higher electronic states of pentacene and also include the tetracene monomer in the study. Table 1 gives selected results for the excited states of the pentacene monomer, while Table S8 summarizes the corresponding data for the tetracene monomer. More data for pentacene are given in Table S3. For pentacene, [14,14]CASPT2 was chosen as the reference method. To maintain consistency with respect to the number of  $\pi$  electrons in the active space, we used a [10,10]CASPT2 approach for tetracene. The involved MOs for pentacene are sketched in Tables S4 and S5. The corresponding MOs for tetracene are recovered by removing the portion of the central six-membered ring from the pentacene MOs. The most important configurations of the CASSCF wave functions for the various states are given in Table S6. The configurations for tetracene follow the same pattern, albeit with a smaller CAS space. More information about the electronic characteristics of the various states can be found in the literature summarized in Tables 2 and S9.

Consistently, all methods predict that for both acene molecules, the equilibrium geometry of the  $S_1$  state is slightly elongated compared to the  $S_0$  geometry (Figure S1). The magnitude of this variation depends on the chosen methodology, but the differences between the methods remain relatively small (Figures S2). For example, in the case of pentacene, [14,14]CASSCF/ANO-S-VDZP predicts an elongation along the long molecular axis of 0.02 Å, while B3LYP/6-31G\* and  $\omega\text{B97X-D3/def2-TZVP}$  both predict a slightly larger variation of 0.06 Å. This elongation is in line with the nodal



**Table 1. Excitation Energies Computed for the Pentacene Monomer<sup>a</sup>**

method/basis set	excitation	$S_1$ [eV]	$S_2$ [eV]	$S_3$ [eV]
B3LYP/6-31G*	Vert.	2.05		3.07
	Adiab.	1.80		2.84
	0–0	1.75		2.72
CAM-B3LYP/6-31G*	Vert.	2.44		3.57
	Adiab.	2.17		3.44
	0–0	2.10		3.35
$\omega$ B97X-D3/def2-SVP untuned	Vert.	2.56		3.59
	Adiab.	2.28		3.45
	0–0	2.20		3.37
$\omega$ B97X-D3/def2-SVP tuned	Vert.	2.38		3.52
	Adiab.	2.10		3.36
	0–0	2.03		3.26
$\omega$ B97X-D3/aug-cc-pVDZ untuned	Vert.	2.45		3.54
	Adiab.	2.18		3.42
	0–0	2.13		3.35
$\omega$ B97X-D3/aug-cc-pVDZ tuned	Vert.	2.29		3.47
	Adiab.	2.01		3.31
	0–0	1.94		3.21
[14,14]CASPT2 (SS,Im.0.1)/ANO-S-VDZP	Vert.	2.48	2.94	3.74
	Adiab.	2.28	2.54	3.76
	0–0	2.21		3.66
[14,14]CASPT2 (SS,Im.0.1)/aug-cc-pVDZ	Vert.	2.41	2.90	3.72
	Adiab.	2.19	2.57	3.80
	0–0	2.12		3.70
$\omega$ PBE/6-31+G* untuned	Vert.	2.58		3.55
$\omega$ PBE/6-31+G* tuned	Vert.	2.36		3.46
$\omega$ PBEh/6-31+G* untuned	Vert.	2.47		3.56
$\omega$ PBEh/6-31+G* tuned	Vert.	2.37		3.52
CC2/cc-pVTZ	Vert.	2.44		3.35
SCS-CC2/cc-pVTZ	Vert.	2.67		3.33
ADC(2)/cc-pVTZ	Vert.	2.43		3.35
SCS-ADC(2)/cc-pVTZ	Vert.	2.64		3.33
DLPNO-STEOM-CCSD/cc-pVTZ	Vert.	2.43		2.91

<sup>a</sup>For CASPT2, the 0–0 energies were computed using the CASSCF geometries for the adiabatic energies and the vibrational contributions of the corresponding  $\omega$ B97X-D3 approach.

**Table 2. Calculated and Measured Pentacene Monomer Excitation Energies from the Literature**

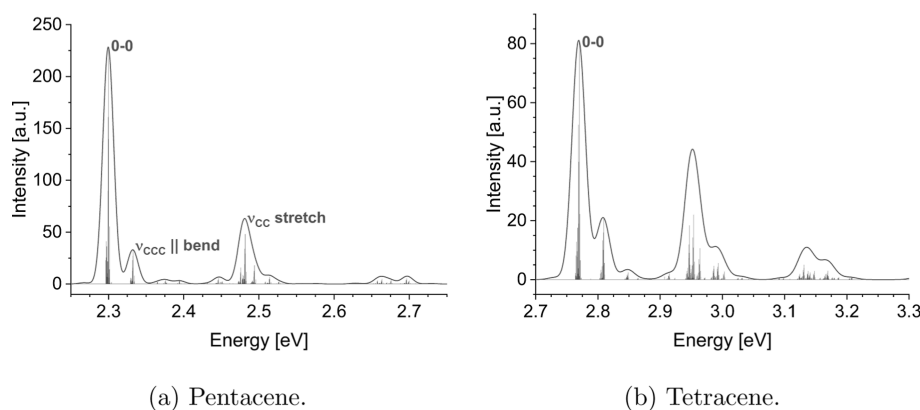
reference	method	excitation	$S_1$ [eV]	$S_2$ [eV]	$S_3$ [eV]
Coto et al. <sup>70</sup>	[14,14]CASPT2/ ANO-L-VTZP	Vert.	2.31	2.88	3.14
Marian and Gilka <sup>71</sup>	DFT-CI/SV(P)	Vert.	2.22		2.96
Halasinski et al. <sup>72</sup>	Exp. (neon matrix)	0–0	2.28		3.73
Heinecke et al. <sup>73</sup>	Exp. (vacuum)	0–0	2.31		
Biermann and Schmidt <sup>69</sup>	Exp. (solution, 0–0-corrected)	0–0	2.23		4.14

structures of the orbitals involved (HOMO  $\rightarrow$  LUMO, see Table S4). DLPNO-STEOM-CCSD/def2-TZVP single-point calculations indicate that the CASSCF-predicted geometries for  $S_1$  are the most accurate for both molecules, although the energy differences are less than 0.1 eV. Furthermore, for the ground states, the energy differences are even smaller, being

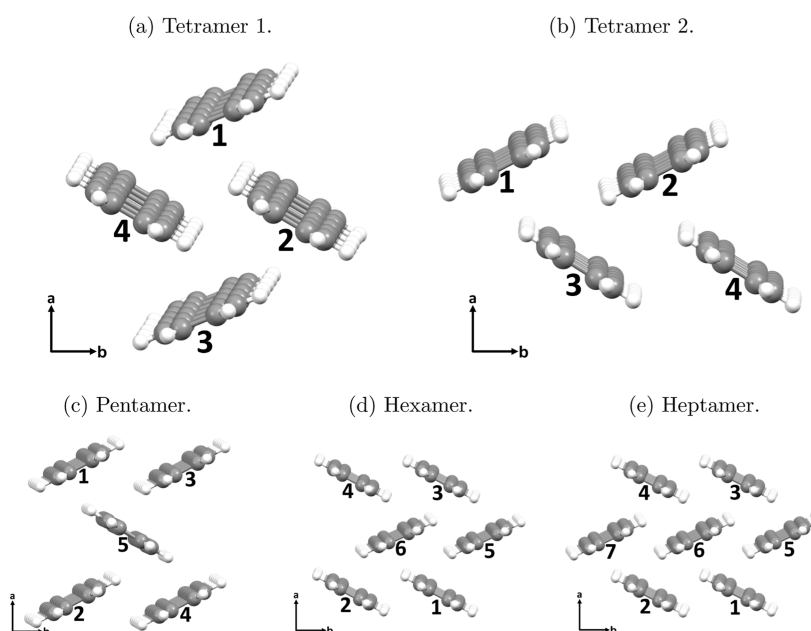
less than 0.01 eV. Despite the minor geometric adjustments, these relaxations lower the  $S_1$  state by 0.2–0.3 eV. Additional vibrational effects (0–0), which were solely computed at the TD-DFT level, have a smaller impact ( $\leq 0.05$  eV). Taking both effects into consideration, the computed 0–0 transitions are about 0.3 eV lower than the vertical energies. Consequently, the use of simple vertical energies is expected to result in overestimated excitation energies when compared to experimental values (see Tables 2 and S9). This observation aligns with similar errors reported by Jacquemin<sup>74</sup> for vertical energies in a set of small molecules.

For pentacene, the best agreement between the computed and the experimental 0–0 excitation energies of 2.28<sup>72</sup> to 2.31 eV<sup>73</sup> (see Table 2) is found with the [14,14]CASPT2-(SS,im.0.1)/ANO-S-VDZP approach, which deviates less than 0.1 eV. Using the aug-cc-pVDZ basis set, the calculated excitation energy decreases slightly so that a deviation of 0.16 eV is found. If the CAS space is decreased stepwise from [14,14] to [4,4], the calculated excitation energy oscillates by about 0.2 eV. An accuracy similar to that of [14,14]CASPT2 is found with the untuned  $\omega$ B97X-D3 functional, which also deviates less than 0.1 eV if the def2-SVP basis set is used. The corresponding aug-cc-pVDZ computation influences the values similar to the [14,14]CASPT2 approach. A comparison of the CASPT2 wave functions with the corresponding TD-DFT natural transition orbitals shows that both methods predict the same electronic character for  $S_1$ , i.e., a HOMO  $\rightarrow$  LUMO excitation (Tables S4 and S5). While the untuned  $\omega$ B97X-D3 functional provides a similar accuracy to that of the much more elaborate [14,14]CASPT2 approach, rather surprisingly, the tuned  $\omega$ TB97X-D3 functional does not improve the calculated excitation energy. On the contrary, the calculated values are about 0.2 to 0.3 eV too low. Other tunable range-separated functionals such as  $\omega$ PBE and  $\omega$ PBEh yield similar trends and results. The untuned range-separated CAM-B3LYP functional with the 6-31G\* basis set produces energies similar to those of  $\omega$ TB97X-D3, i.e., slightly too low. The commonly used B3LYP/6-31G\* combination consistently predicts vertical and 0–0 transitions that are approximately 0.5 eV lower than the experimental values. This discrepancy highlights the limitations of this particular functional. Interestingly, there is a favorable error compensation when comparing vertical energies (2.05 eV, see Table 1) with experimental 0–0 transitions (2.28 eV, see Table 2) for this combination. High-accuracy wave function-based methods like ADC(2), CC2, and DLPNO-STEOM-CCSD provide vertical excitation energies of around 2.4 eV, in good agreement with the CASPT2 predictions. The inclusion of SCS for CC2 and ADC(2) leads to vertical transitions around 0.2 eV higher. This underlines the accuracy of the approaches as discussed in the literature.<sup>39,51,75,76</sup>

The  $S_2$  state of pentacene represents a double excitation (HOMO<sup>2</sup>  $\rightarrow$  LUMO<sup>2</sup>) that is not accessible with linear response approaches such as TD-DFT, CC2, or ADC(2).<sup>78,79</sup> Due to its nature, the state is dark and cannot be observed by linear absorption spectroscopy. For pentacene, our CASPT2 calculations agree well with earlier works by Coto et al.<sup>70</sup> (see Table 2). The geometry of the  $S_2$  state of pentacene obtained by CASSCF optimization exhibits a similar elongation along the long molecular axis as observed in the  $S_1$  state. However, this elongation is even more pronounced in the higher excited states. This heightened elongation is anticipated as the



**Figure 1.** Vibrationally resolved spectra of the pentacene and tetracene monomers in the gas phase computed with  $\omega$ B97X-D3/def2-SVP and ezFCF 1.1.<sup>77</sup> More information about the individual transitions can be found in Table S6. A Gaussian broadening of 25 meV is included to mimic experimental broadening effects.



**Figure 2.** Geometries of the clusters used to mimic the absorption spectrum of pentacene thin films, taken from previous work by the authors.<sup>20</sup>

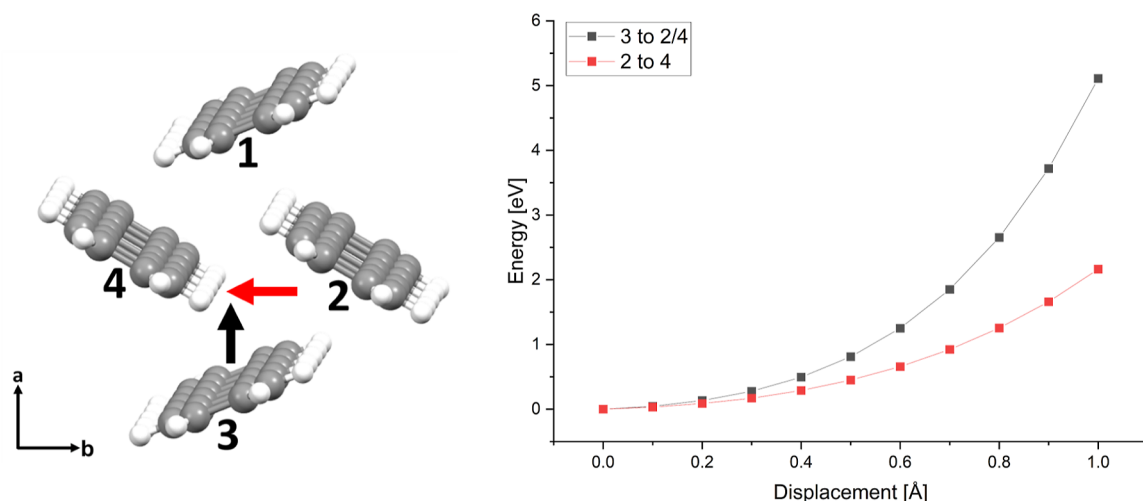
transitions involve the same orbitals but entail double excitations instead of single excitations.

The  $S_3$  state of pentacene is well described by [14,14]-CASPT2, which deviates by  $\leq 0.2$  eV from the experimental value by Halasinski et al.<sup>72</sup> of 3.73 eV. The experimental value given by Biermann and Schmidt<sup>69</sup> seems to be too high, taking into account that this value was extrapolated from solution spectra. According to the CASSCF wave function, the  $S_3$  state also exhibits some double excitation character. This observation may help explain why linear response approaches yield larger errors compared with those found for the  $S_1$  state. The predictions from  $\omega$ B97X-D3 or CAM-B3LYP lie at least 0.4 eV too low. Based on their vertical energies, the PBE-based functionals give comparable errors. CC2, SCS-CC2, and SCS-ADC(2) produce quite accurate vertical excitation energies for the  $S_3$  state (deviation  $\approx 0.1$  eV), while the excitation energies predicted by ADC(2) and DLPNO-STEOM-CCSD lie 0.2 eV lower. All of these methods consistently predict excitation energies that are too low in comparison to the available 0–0 experimental transition. Similar deviations are found for previous calculations by Coto et al.<sup>70</sup> and Marian and

Gilka<sup>71</sup> (Table 2). It is important to note that the absorption spectra measured for pentacene or tetracene thin films mainly focus on an energy range where only  $S_1$  linear combinations of the monomers are important. Therefore, a good description of the  $S_1$  state, as indeed given by TD-DFT, should be sufficient for describing the photophysics of the thin films, as well.

Figure 1 depicts the vibrationally resolved  $S_0 \rightarrow S_1$  spectra of pentacene (a) employing  $\omega$ B97X-D3/def2-SVP in combination with the ezFCF 1.1 program.<sup>77</sup> It agrees with its experimental counterparts (Table S7). The influence of the chosen xc-functional (untuned or tuned) on the shape of the spectrum is negligible. Using the Herzberg–Teller model in addition to Franck–Condon transitions has no influence on the spectral shapes of either molecule.

For a detailed discussion of the tetracene monomer, see Supporting Information Section S2. The general trends and findings coincide with those for pentacene. Due to its importance for the cluster calculations, we would only like to point out that the vibrational progression found for pentacene (Figure 1a) is less pronounced than that of tetracene (Figure 1b). This difference can be seen best by the higher relative



**Figure 3.** PECs for pentacene as a function of the displacement of monomers 2 (red arrow) and 3 (black arrow), respectively. The PECs are color coded according to the arrows. The 0.0 point indicates the intermonomeric distances taken from the crystal structure.

intensity of the absorption peak in the tetracene spectrum located about 0.2 eV above the 0–0 peak compared to its corresponding peak in the pentacene absorption spectrum. A similar variation is found for the  $\nu_{\text{CCC}}$  peaks.

**3.2. Cluster Selection and the Approach to Consider Photoinduced Relaxation Effects.** The clusters of pentacene and tetracene depicted in Figures 2 and S4 were employed to investigate whether and how cluster structures influence the calculated (polarization-resolved) absorption spectra. We started with the herringbone dimer (monomers 1 and 2 of the tetramer 1 cluster) and enlarged the clusters to up to seven monomers to investigate how the number of monomers influences the spectrum. To analyze how the spatial arrangement changes the spectra for the pentacene tetramer, we computed two different clusters (Figure 2a,b). Unless otherwise stated, the monomer structures within a given cluster are identical. To compute resulting differences, we also investigated a cluster in which one monomer adopts a different geometry, thereby breaking possible symmetries. As initial calculations indicate similar trends for pentacene and tetracene, fewer clusters were tested for tetracene. The clusters used for perylene are discussed later.

For the monomer, vertical excitations were found to overestimate the excitation energies by up to 0.4 eV. To analyze such effects, we studied photoinduced inter- as well as intramonomer geometry relaxation. To investigate possible intermonomeric effects, we computed the potential energy curves (PECs) as a function of the distances indicated in Figure 3 (left). In these computations, the intramonomeric geometrical parameters were kept frozen. The corresponding color-coded PECs of the ground state are given in Figure 3 (right), while those of other bright states are shown in Figures S5–S7. The 0.0 Å displacement represents the intermonomeric distances extracted from the crystal structure. The PECs indicate that the crystal structure represents the minimum energy geometry for all electronic states with respect to these intermonomer coordinates. Therefore, no photoinduced intermonomeric relaxation is expected. Additionally, all PECs exhibit a high degree of flatness, consistent with the experimental finding that lattice vibrations have magnitudes below  $100 \text{ cm}^{-1}$  (0.01 eV).<sup>80,81</sup> Furthermore, as the PEC shapes are very similar for all states, 0–0 transitions are

expected. Hence, we have chosen to neglect intermonomeric relaxation effects as well as the corresponding lattice vibrations, as their impact would be well below the accuracy of our quantum chemical approach ( $\leq 0.1$  eV).

Intramonomeric relaxation effects might be more important since they influence the excitation energies of pentacene and tetracene monomers by 0.3–0.4 eV. To circumvent problems arising from missing steric restrictions, the monomer geometries were modulated linearly from the equilibrium ground-state geometry of the monomer ( $\vec{R}(S_0)$ ) to the equilibrium geometry in its  $S_1$  state ( $\vec{R}(S_1)$ ) using

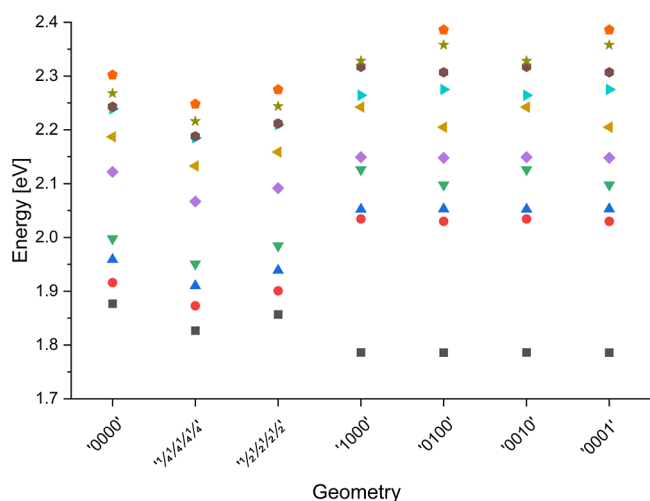
$$\vec{R}_\chi = \vec{R}(S_0) + \chi \Delta \vec{R} \quad (3)$$

with

$$\Delta \vec{R} = \vec{R}(S_0) - \vec{R}(S_1) \quad (4)$$

$\chi$  was varied from  $-0.5$  to  $1.5$  in steps of  $0.25$  for each monomer of the cluster. According to eq 3,  $\chi = 0.0$  gives  $\vec{R}(S_0)$  while  $\vec{R}(S_1)$  is obtained with  $\chi = 1.0$ . While varying the intramonomer geometries, the intermonomer orientations were fixed. An enlarged description of the difference between  $\vec{R}(S_0)$  and  $\vec{R}(S_1)$  is given in Figure S1. To indicate monomer distortions, the  $\chi$  value for each monomer in a cluster is given. Consequently, 0000 means that all monomers remain in the  $\vec{R}(S_0)$  geometry, while  $\frac{1111}{4444}$  indicates that each monomer was distorted with  $\chi = 0.25$ . Clusters in which all monomers adopt the same geometry are called symmetric clusters. Finally, 1000 means that the first monomer is in the  $\vec{R}(S_1)$  geometry, while all others remain in the  $\vec{R}(S_0)$  geometry. In such clusters, the symmetry is broken; hence, they will be called asymmetric clusters.

Figure 4 displays the relative energies of the lowest singlet excited states for various geometries compared to the 0000 ground-state energy (0 eV on the energy scale) within tetramer cluster 1. These energies effectively illustrate the potential energy surfaces (PESs) of tetramer cluster 1 as the  $S_0$  geometries of selected monomers transition to  $S_1$  geometries. The monomer data were obtained using optimally tuned  $\omega_T$ B97X-D3 ( $\omega = 0.11 \text{ a.u.}^{-1}$ ) in combination with def2-SVP



**Figure 4.** Energetic behavior of the lowest ten singlet excited states of the tetramer 1 cluster of pentacene as a function of different geometries ( $\omega_1$ B97X-D3/def2-SVP + C-PCM). All energies are relative to the ground-state energy of the 0000 geometry. See the text for more information.

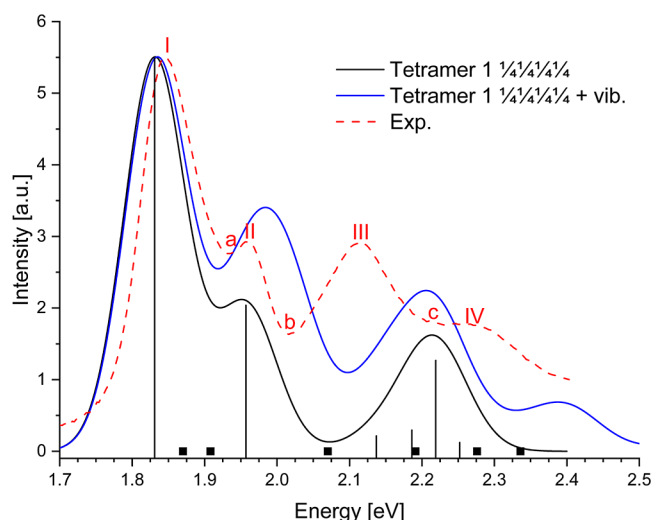
basis sets. The plot reveals interesting insights: when each monomer is distorted by a quarter toward the  $\bar{R}(S_1)$  configuration ( $\frac{1111}{4444}$ ), the  $S_1$  energy of the cluster becomes around 0.05 eV lower than for that of the 0000 and  $\frac{1111}{2222}$  geometries. This behavior is consistent across all considered excited states, indicating that  $\frac{1111}{4444}$  represents a local minimum on the PES. Transitioning from a  $\frac{1111}{4444}$  to a 1000 configuration results in a further 0.05 eV reduction of the  $S_1$  state energy, indicating that 1000 represents the global minimum of the  $S_1$  PES. For all other excited states under consideration, the 1000 geometry is consistently 0.1–0.2 eV higher in energy, implying that  $\frac{1111}{4444}$  represents a global minimum for these states. Additionally, Figure 4 illustrates that 1000 and 0010, as well as 0100 and 0001, are energetically degenerate with only minute differences between them. This observation indicates the presence of symmetries within the cluster and proves that in tetramer 1, the environments of all monomers are highly similar.

The relevance of vibronic states arising from intramonomer vibrations on the optical properties of molecular crystals has been highlighted in various studies.<sup>3,5</sup> Therefore, it is essential to consider such effects. Although the intermolecular interaction between monomers within a thin-film OSC is relatively weak, it is important to investigate whether this interaction significantly influences the vibrational progression of the thin film in comparison to that of the monomer. To address this concern, careful measurements of vibrational Davydov-splittings and collective mode polarizations were conducted in oriented crystals of perfluoropentacene (PFP) crystals by Breuer et al.<sup>82</sup> The measurements were then compared to DFT calculations by employing periodic boundary conditions. Both experiment and theory indicated that the effects are minimal. The computations predicted that the mode splitting ranged within 0–37  $\text{cm}^{-1}$ , closely aligning with the experimental findings (2–33  $\text{cm}^{-1}$ ). Additionally, for most splittings, only one of the bands exhibited an intensity

similar to the original monomer vibrations, while the intensities of the other bands were suppressed. Shifts in the energy positions of the bands due to the crystal environment varied between 0 and 20  $\text{cm}^{-1}$ . Importantly, the magnitudes of both effects are significantly smaller than the error bars associated with the electronic structure methods used in the present study ( $\leq 0.1$  eV). Considering that additional intermonomeric modes possess relatively low energy, it can be inferred that the undisturbed monomer vibrations already provide reasonable approximations to the vibrational modes of the crystal. Therefore, we overlaid each electronic transition with the vibrational progression of the monomer, as sketched in Figure S8. We used the Franck–Condon approximation, i.e., the intensities of the vibrations were weighted by the intensity of the respective electronic transition.

### 3.3. Absorption Spectra of Symmetric $\frac{1111}{4444}$ Tetramer 1 Clusters of Pentacene and Tetracene and the Assignment of the Respective Spectra.

The calculated total absorption spectra for the pentacene tetramer 1 in the  $\frac{1111}{4444}$  geometry are shown in Figure 5. Neglecting vibrational

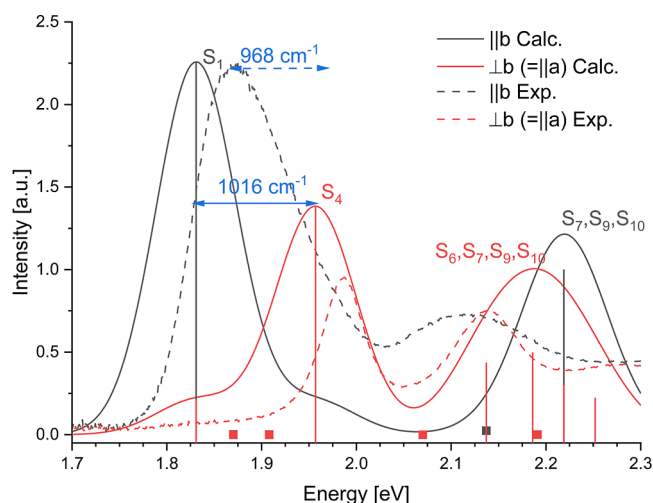


**Figure 5.** Absorption spectrum computed for pentacene tetramer 1. The energetic positions of the electronic states are marked by bars reflecting the calculated relative intensities. States with vanishing intensities are marked by squares, taken from previous work by the authors.<sup>20</sup>

effects, the band structure up to 2.3 eV is in excellent agreement with that of the experiment. The energy positions of both lowest bands differ by less than 0.03 eV from their experimental counterparts, while the third band is blue-shifted by about 0.07 eV. This larger deviation can be explained via the character of the underlying state (see below). The fourth band in the experimental spectrum at about 2.3 eV is missing. It appears at about 2.4 eV when vibrational effects are included. This additionally influences the position of the second band by blue-shifting it by about 0.03 eV and increasing its intensity in comparison to that of the lowest band. Overall, apart from the appearance of the additional band, the influence of the vibrational effects on the computed pentacene absorption spectra seems to be small.

The computed polarization resolved spectrum given in Figure 6 is also in excellent agreement with the experimental counterpart. The deviation found for the Davydov-splitting is





**Figure 6.** Polarization-resolved optical absorption spectra computed for pentacene tetramer 1. The Davydov-splitting is indicated, taken from previous work by the authors.<sup>20</sup>

less than  $50\text{ cm}^{-1}$ . Differences between the computed (Figure 6) and experimental polarization-resolved spectra might result from temperature effects. While the calculations in this work were of course carried out at 0 K, the experimental spectra were recorded at room temperature.<sup>9</sup> Available literature<sup>83–85</sup> shows slight red shifts in peak positions when lowering the temperature. For extremely thin films grown on ZnO, the trend is reversed, but this is due to the growing influence of ZnO, which is not included in our calculations. Helzel et al.<sup>84</sup> found that for a 100 nm thick layer, the  $E^+$  Davydov component (Figure 6 dashed black line) shows a red shift of 0.011 eV, while the red shift of the corresponding  $E^-$  component (Figure 6 dashed red line) is slightly smaller (0.005 eV). As a consequence, the Davydov-splitting increases by about  $50\text{ cm}^{-1}$ . Additionally, both components are red-shifted. Hence, including temperature effects would most likely further improve the agreement between theory and experiment.

Excitation energies, transition dipole moments, and electron–hole (e–h) correlation plots for the underlying excited states are given in Table 3, and more descriptors are included in Table S10. For the  $\frac{1111}{4444}$  situation, the delocalization of the excited states is from the e–h correlation plots (Table 3) and the PR values (Table S8). The lowest four excited states ( $S_1$ – $S_4$ ) are mainly Frenkel states, while the ones above have a predominantly CT character. Moreover, there are a number of dark states in the considered energy range. The troughs in the absorption spectra are therefore not caused by the absence of states in this energy range but by states with vanishing transition dipole moments. More information about pentacene can be found in ref 20.

The same methodology as that described for pentacene was now used for tetracene. Using the tetramer 1 cluster in its  $\frac{1111}{4444}$  geometry leads to very good agreement for both total (Figure 7) and polarization-resolved (Figure 8) spectra when the vibrational progression of a monomer is added to the peaks. The main difference from pentacene is that a whole discrete band (II) appears only when the vibrational approximation is applied. This is consistent with experimental reports attributing absorption band II to a vibronic progression

based on the observation of equal shifts in absorption band Ib and II upon application of an external pressure.<sup>86</sup>

Davydov-splitting is obtained with a similar accuracy to that of pentacene (error around  $80\text{ cm}^{-1}$ ). Because of the nature of our vibrational approximation, the Davydov splitting of band II is exactly the same as that for band I due to the second peaks in the polarization-resolved spectra also stemming from monomer vibrations. The information on the nature of the excited states is summarized in Tables S11 and S12. As for pentacene, the first four states of the tetracene spectrum represent mainly Frenkel states. Again, they are distributed throughout the cluster, but monomers 2 and 4 possess slightly higher contributions to the  $S_1$  state while monomers 1 and 3 are more strongly represented in the  $S_2$  state. These small differences with respect to pentacene are due to the fact that the tilt angle of the monomers in the tetracene crystal deviates more from  $90^\circ$  than in the case of pentacene. In addition, the stronger deviation of the crystal lattice angle  $\gamma$  from  $90^\circ$  in tetracene probably contributes to the nonuniform distribution of the exciton on the molecules composing the tetramer cluster.

The results of calculations for tetramer 1 of both pentacene and tetracene can now be used to assign the experimental peaks to distinct electronic transitions (Tables 4 and 5).

Peak I of the pentacene spectrum corresponds to the Frenkel  $S_1$  state with an approximately 30% CT admixture. This is in agreement with previous assignments.<sup>5,23</sup> The second band stems from the pure Frenkel state  $S_4$  and the third one mainly to the pure CT state  $S_9$  with less intensive contributions of the  $S_6$ ,  $S_7$ , and  $S_{10}$  CT states. Band IV in our model emanates from the vibrational progression of the CT peak III. For the higher bands, our interpretation deviates from Beljonne et al.,<sup>5</sup> who assigned all peaks higher in energy than the first to vibrational progressions. The assignment from Sebastian et al.<sup>23</sup> matches ours with the exception of band IV, which they allocated to an additional CT state.

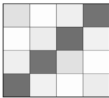
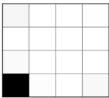
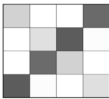
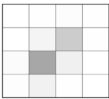
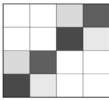
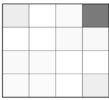
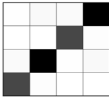

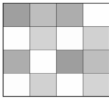
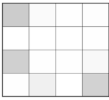

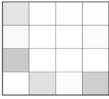
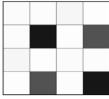
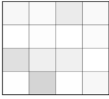
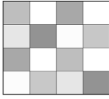
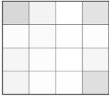
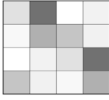
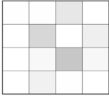
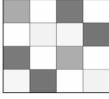
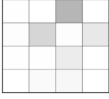
For tetracene, the first peak shows the expected two Davydov components (Ia and Ib), which correspond to the  $S_1$  and  $S_4$  states in our model. The  $S_1$  state possesses a mainly Frenkel character with 20% CT admixture while the  $S_4$  state has a pure Frenkel character. Peak II originates from the vibrational progression of band I. The CT states  $S_6$ ,  $S_7$ , and  $S_9$  form peak III of the spectrum. The fourth band emanates from the vibrational progression of band III, as was the case for pentacene, as well. Our assignment agrees with the literature for the bands Ia and Ib, which are also attributed to electronic transitions.<sup>3</sup> In contrast, in line with our findings, band II was assigned to a vibronic progression based on the observation of equal shifts in absorption band Ib and II upon application of an external pressure.<sup>86</sup> Therefore, on comparison with pentacene, the larger homologue of tetracene also implies that absorption band III in pentacene is likely to result from optical transitions to electronic states and vibrational progressions of lower lying electronic states. While the former is justified by the numerous electronic states found in our simulations, the latter would agree with the experimental results reported in ref 88.

### 3.4. Influence of Relaxation Effects and Cluster Size.

Figure 9 shows the calculated electronic absorption spectra for the pentacene tetramer 1 in the crystal structure and 0000 and  $\frac{1111}{4444}$  geometries. The relative energetic positions of the bands and the intensities of the vertical spectrum (0000) and of the  $\frac{1111}{4444}$  distortion are very similar and the 0000 spectrum is only



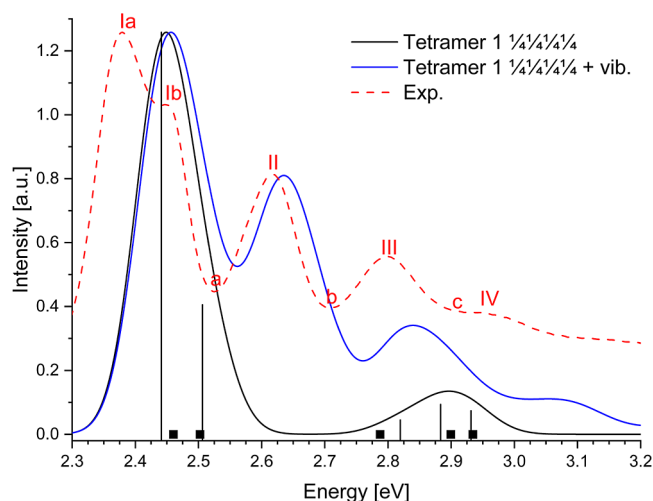
Table 3. Characterization of the Lowest Ten Singlet Excited States of the Pentacene Tetramer  $\frac{1111}{4444}$  and 1000 in PCM

$S_x$	E [eV]	$\mu_{i \rightarrow f}$ [D]	$\frac{1111}{4444}$ e-h-correlation plot	E [eV]	$\mu_{i \rightarrow f}$ [D]	1000 e-h-correlation plot
1	1.83	3.01		1.79	2.00	
2	1.87	0.00		2.03	2.17	
3	1.91	0.00		2.05	1.03	
4	1.95	1.83		2.13	1.49	
5	2.07	0.00		2.15	0.24	
6	2.13	0.61		2.21	0.21	
7	2.19	0.71		2.28	0.63	
8	2.19	0.00		2.31	1.61	
9	2.22	1.44		2.36	0.18	
10	2.25	0.43		2.39	0.22	

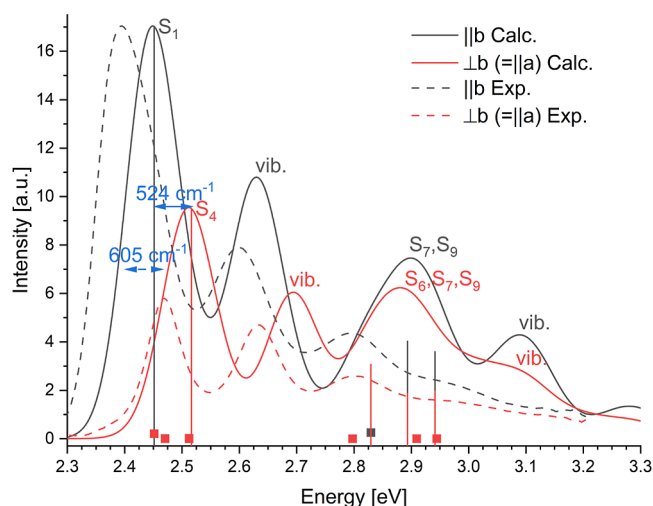
blue-shifted by 0.05 eV. The spectrum is even reproduced when using an unoptimized crystal structure; it is just further blue-shifted by 0.02 eV in comparison to the 0000 spectrum.

While the variations in absorption spectra between the  $\frac{1111}{4444}$ , the 0000, and the crystal structure of the pentacene cluster tetramer 1 (Figure 2) are small, the differences between the spectra calculated for the  $\frac{1111}{4444}$  (Figure 5) and the 1000 geometries (Figure 10a) are tremendous. For the 1000 geometry, neither total nor the polarization-resolved spectra show any resemblance to their respective experimental counterparts. The reason for the strong variation is a localization of the exciton in the  $S_1$  state. For the  $\frac{1111}{4444}$  geometry, it is delocalized over the whole cluster, but for the

1000 geometry it localized on monomer 1, i.e. on the monomer which adopted the equilibrium geometry of the  $S_1$  state of the monomer. This localization can clearly be seen on the corresponding e–h correlation plots in Table 3 and the PR values (Table S10). Comparing the excitation energies of 1000 to  $\frac{1111}{4444}$ , the main difference lies in the energy gap between  $S_1$  and  $S_2$ , which is about 0.04 eV for the  $\frac{1111}{4444}$  geometry but about 0.2 eV for 1000. It results since the 1000 geometry represents the minimum structure for the  $S_1$  state but is higher in energy than the  $\frac{1111}{4444}$  geometry for all other states, as shown in Figure 4. The main difference between the spectra arises from the computed intensities, which differ strongly for all states. For the 1000 geometry, the bright-dark intensity



**Figure 7.** Absorption spectrum computed for tetracene tetramer 1. Experimental spectra taken from Zeiser et al.<sup>24</sup> The energetic positions of the electronic states are marked by bars reflecting the calculated relative intensities. States with vanishing intensities are marked by squares.



**Figure 8.** Polarization-resolved optical absorption spectra computed for tetracene tetramer 1 including vibrational effects. The Davydov-splitting is indicated. The experimental spectra are taken from Valencia et al.<sup>12</sup>

pattern of the transitions is therefore completely broken, which results from the now asymmetric structure of the cluster possessing a symmetry-breaking element leading to the wrong spectra.

Therefore, although the asymmetric 1000 geometry represents the minimum for the  $S_1$  state, the missing resemblance to the experimental data (see Figure 10a) indicates that during the measurement of the absorption spectrum, the excitons in the thin films of pentacene and tetracene remain delocalized instead of localizing on one monomer. After absorption, a localization might take place on a longer time scale, as was reported by Wirsing et al.<sup>14</sup> The 1000 geometry could therefore be of interest when photo-induced relaxation effects are investigated. The 1000 distortion of tetramer 1 of tetracene leads to the same erroneous behavior as observed for pentacene (Figure 10b and Tables S11 and S12).

**Table 4.** Assignment of the Absorption Spectrum of Pentacene (Figure 5)<sup>a</sup>

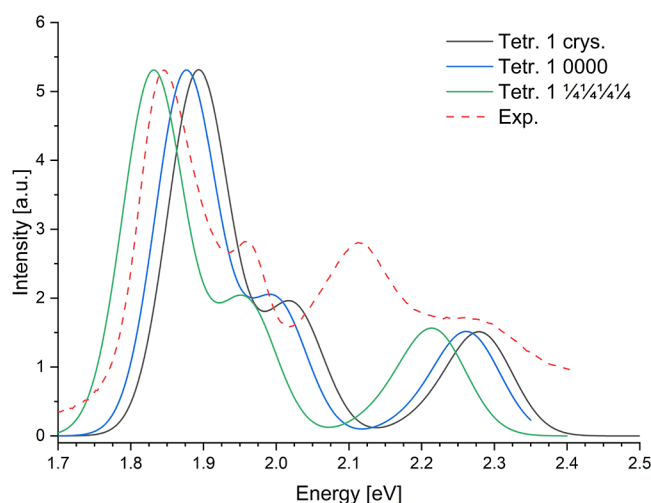
peak/valley	$E_{\text{exp}}$ [eV] <sup>87</sup>	$E_{\text{calc}}$ [eV]	state	$T^2$ [a.u. <sup>2</sup> ]	$T  b$ [a.u.]	$T\perp b$ [a.u.]
I	1.87	1.83	$S_1$	5.48	2.27	0.21
		1.87	$S_2$	0	0	0
		1.91	$S_3$	0	0	0
II	1.97	1.95	$S_4$	2.04	0.21	1.39
		2.07	$S_5$	0	0	0
III	2.12	2.13	$S_6$	0.21	0.03	−0.45
		2.19	$S_7$	0.29	0.14	0.52
		2.18	$S_8$	0	0	0
		2.22	$S_9$	1.27	1.01	−0.32
		2.25	$S_{10}$	0.12	0.18	−0.23
c						
IV	2.27	2.38	Vib.			

<sup>a</sup> $T$  is the transition dipole moment.

**Table 5.** Assignment of the Absorption Spectrum of Tetracene (Figure 7)<sup>a</sup>

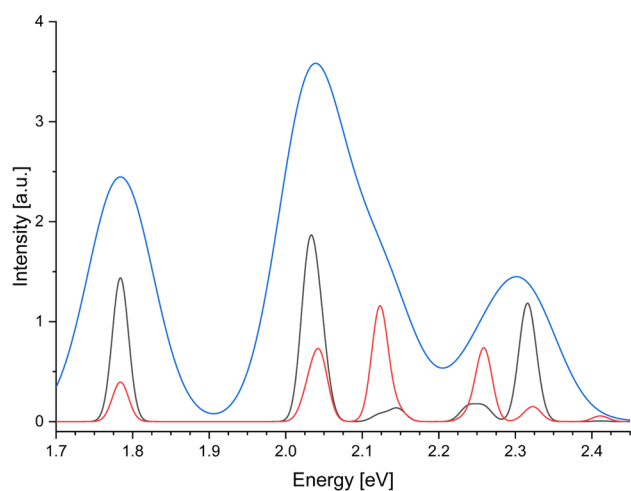
peak/valley	$E_{\text{exp}}$ [eV]	$E_{\text{calc}}$ [eV]	state	$T^2$ [a.u. <sup>2</sup> ]	$T  b$ [a.u.]	$T\perp b$ [a.u.]
Ia	2.38	2.44	$S_1$	5.60	−2.31	0.03
Ib	2.45	2.5	$S_4$	1.81	−0.15	1.31
II	2.62	2.65	Vib.			
b		2.79	$S_5$	0	0	0
		2.82	$S_6$	0.20	0.03	0.42
		2.81	$S_7$	0.42	0.55	−0.26
		2.93	$S_9$	0.33	0.49	0.27
		2.94	$S_{10}$	0	0	0
c						
IV	2.95	3.08	Vib.			

<sup>a</sup> $T$  is the transition dipole moment.

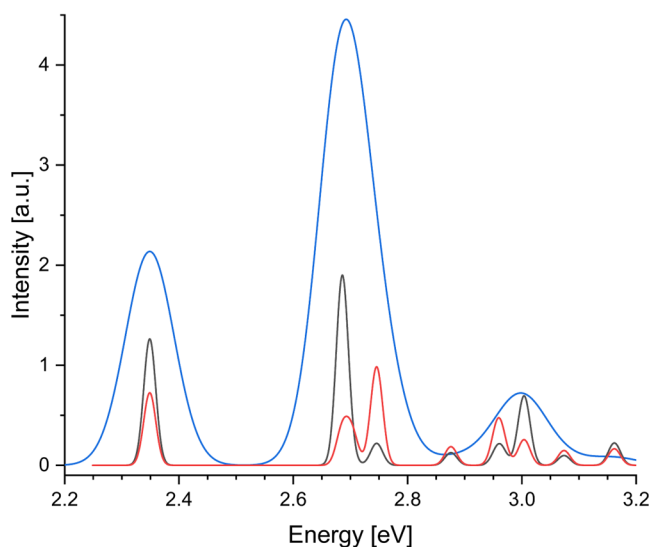


**Figure 9.** Comparison of calculated electronic spectra for the pentacene tetramer 1 for the crystal structure and 0000 and  $\frac{1}{4}\frac{1}{4}\frac{1}{4}$  geometries.

To investigate their dependence on the selection of the cluster, the computed spectra for pentacene tetramer 2, the hexamer, and the herringbone dimer, consisting of monomers 1 and 2 of the tetramer 1 cluster, are shown in Figure 11. More information is given in Supporting Information Sections S7–S9. All of them do not resemble the experimentally measured pentacene thin-film absorption spectrum. This is also the case



(a) Pentacene.

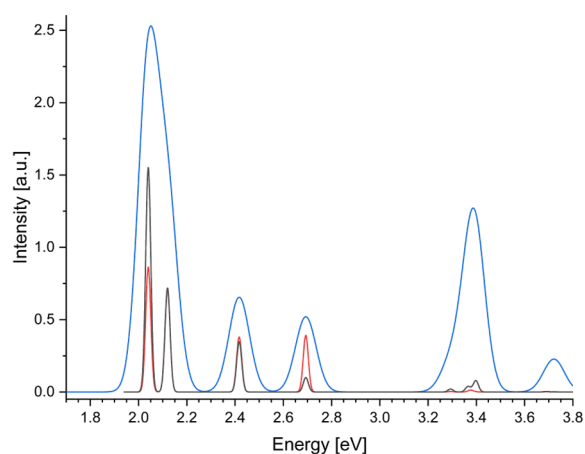


(b) Tetracene.

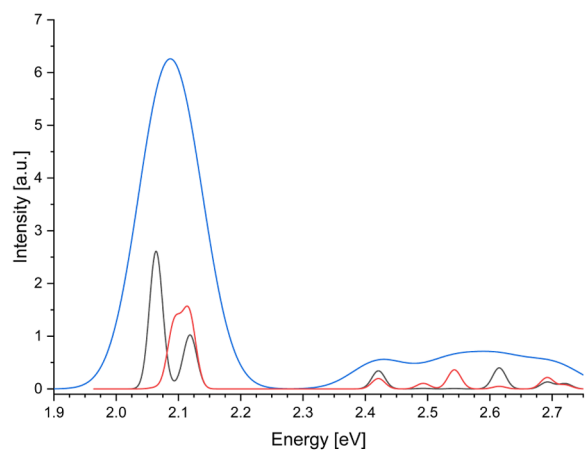
**Figure 10.** Total (blue) and polarization-resolved (black and red) optical absorption spectra computed for pentacene and tetracene tetramer 1 in the 1000 geometry.

for the pentacene heptamer (Supporting Information Section S10) and pentamer (Supporting Information Section S11). For the larger clusters, the computed intensities do not match since the excitons localize on specific monomers. For the dimer, the exciton remains delocalized, but the number of states seems to be too small to describe the spectrum correctly (Table S17). The same observations are made for tetracene tetramer 2 and the hexamer (Supporting Information Sections S7 and S8).

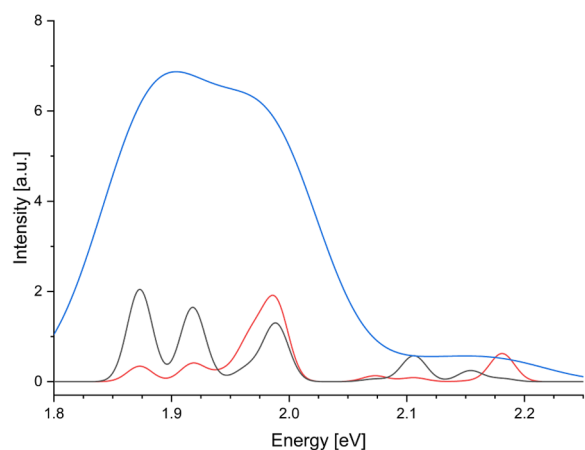
These results shed light on how the cluster should be selected for herringbone crystal structures with a predominant intermolecular interaction within a single molecular plane. A suitable cluster must, of course, reflect the crystal structure, but even more important, the environment of the monomers should be as similar as possible to allow for the formation of delocalized excitons. The former is true for all clusters, but the latter condition is only fulfilled for tetramer 1. For tetramer 2,



(a) Absorption spectrum computed for the pentacene herringbone dimer.



(b) Absorption spectrum computed for the pentacene tetramer 2.



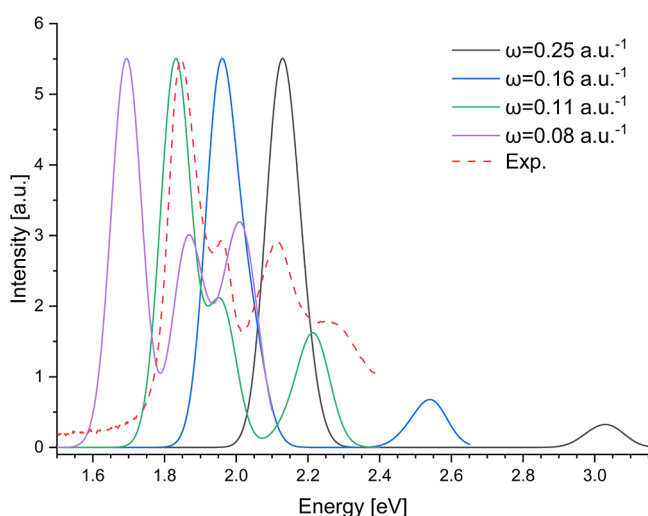
(c) Absorption spectrum computed for the pentacene hexamer.

**Figure 11.** Calculated absorption spectra for different pentacene clusters.



the monomers forming the herringbone dimer in its center (monomers 2 and 3) have three neighbors, while the two outer monomers only have two. This small difference already leads to a preferential localization of the excitons on the inner dimer or the outer monomers (Tables S11 and S12). As a consequence, the computed intensities do not reflect the experimentally observed intensities, so the computed spectra do not show any resemblance to their experimental counterpart. The same reason results in the failure of the hexamer and heptamer, as the central monomer (monomer 6 in Figure 2 and monomer 2 in Figure S2) interacts with more direct neighbors than the outer ones, so the excitations are localized again. Consequently, only tetramer 1 of pentacene and tetracene seems to be appropriate to simulate the absorption spectra of the thin films.

### 3.5. Influence of the Choice of the Range Separation Parameter, Functional, and Basis Sets. Figures 12 and S13



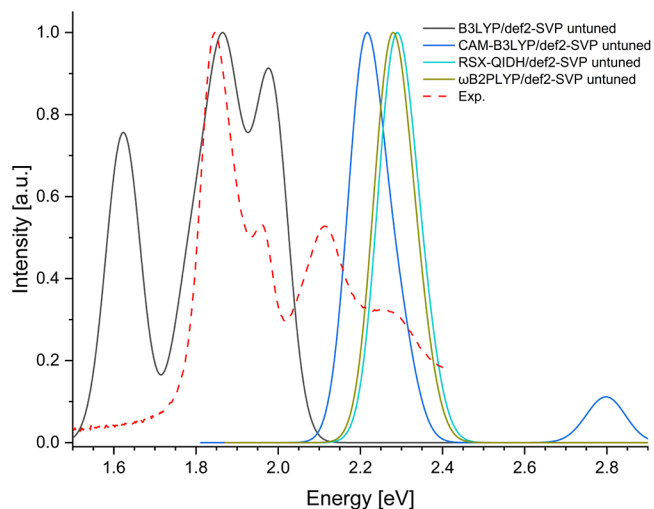
**Figure 12.** Comparison of calculated total electronic absorption spectra of the pentacene tetramer 1 cluster in the  $\frac{1111}{4444}$  geometry (monomers optimized in PCM with  $\omega_T$ B97X-D3/def2-SVP) computed with  $\omega_T$ B97X-D3/def2-SVP for different range separation parameters.

show the total electronic absorption spectra of the pentacene and tetracene tetramer 1 clusters in their  $\frac{1111}{4444}$  distortion for untuned ( $\omega = 0.25$  a.u.<sup>-1</sup>), monomer-tuned ( $\omega = 0.16$  a.u.<sup>-1</sup>), cluster-tuned  $\omega$ B97X-D3 ( $\omega = 0.11$  a.u.<sup>-1</sup>) as well as using an arbitrarily chosen even lower range-separation parameter ( $\omega = 0.08$  a.u.<sup>-1</sup>). The corresponding excitation energies and the characterization of the states are summarized in Tables S20 and S21.

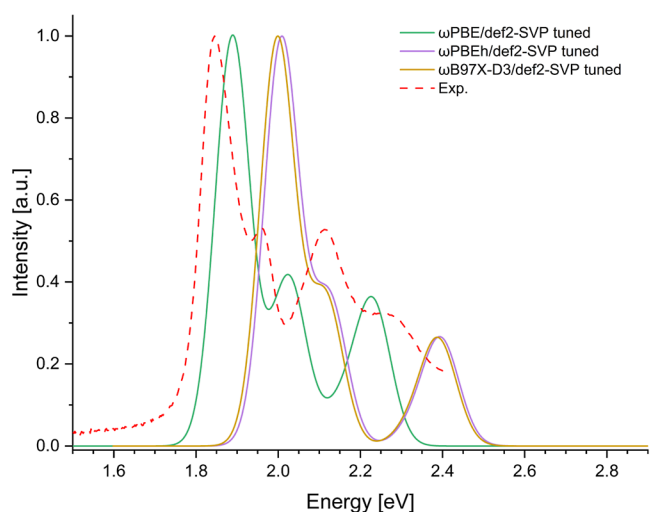
Comparison of the spectra in Figure 12 reveals that tuning of  $\omega$  on the cluster used for the subsequent TD-DFT calculation is decisive for both the energetic range and the shape of the spectrum. The lower the value of  $\omega$  chosen, the more the excitations are shifted to lower energies in the cluster-tuned approach, matching the experiment by far the best. Tables S20 and S21 indicate that lowering  $\omega$  leads to a decreasing energetic distance between the Frenkel and CT states. While the excitation energies of the former decrease only by about 0.2–0.3 eV, those of the latter lower by nearly 1 eV. Due to the decreasing energy difference, the mixing between Frenkel and CT states increases, so that the latter also becomes more

intense (see Supporting Information Section S12). Once more, the sweet spot is hit when using the cluster-tuned functional.

The absorption spectra for the pentacene tetramer 1 in its 0000 geometry obtained with the hybrid functional B3LYP, the untuned range separated hybrid functional CAM-B3LYP, and with the untuned double hybrid functionals RSX-QIDH<sup>89</sup> and  $\omega$ B2PLYP<sup>90</sup> are summarized in Figure 13a. The corresponding



(a) Untuned functionals.



(b) Tuned functionals.

**Figure 13.** Comparison of total absorption spectra of the pentacene tetramer 1 cluster in the 0000 geometry (monomers optimized in vacuum with  $\omega$ B97X-D3/def2-TZVP) computed for the gas phase with different untuned and tuned functionals. The def2-SVP basis set was used for all calculations.

results obtained with the tuned range-separated functionals  $\omega$ PBE,  $\omega$ PBEh, and  $\omega$ B97X-D3 are depicted in Figure 13b. The corresponding spectra for the 1000 geometry in the gas phase are given in Figure S14.

Unsurprisingly, B3LYP and untuned CAM-B3LYP (its tuning failed for both systems since no minimum was found) failed to reproduce the experimental spectrum. The former could be expected since B3LYP was shown to have deficiencies even for the monomer. The incorrect behavior of CAM-B3LYP

results from the untuned version having to be taken. The untuned range-separated double hybrid functionals RSX-QIDH and  $\omega$ B2PLYP show a similar behavior to that of untuned CAM-B3LYP. On the other hand, the tuned range-separated functional  $\omega$ PBE shows good agreement with the experimental shape of the spectrum. The tuned range-separated hybrid functionals  $\omega$ PBEh and  $\omega$ B97X-D3 (both with 20% short-range HF exchange, respectively) show the same correct shape of the absorption spectrum but are blue-shifted by ca. 0.1 eV in comparison to  $\omega$ PBE. In Figure 13, the position of the first peak for  $\omega$ PBE matches the experimental spectrum best. However, this spectrum was calculated for gas phase and the 0000 geometry, i.e. relaxation and solvent effects are neglected. Taking these effects into account, the excitation energies obtained with  $\omega$ B97X-D3 decreased by about 0.15 eV (compare Figures 9 and 13). Assuming similar effects for the other range-separated functionals, an improvement is obtained for  $\omega$ B97X-D3 and  $\omega$ PBEh, while the agreement for  $\omega$ PBE is slightly worse.

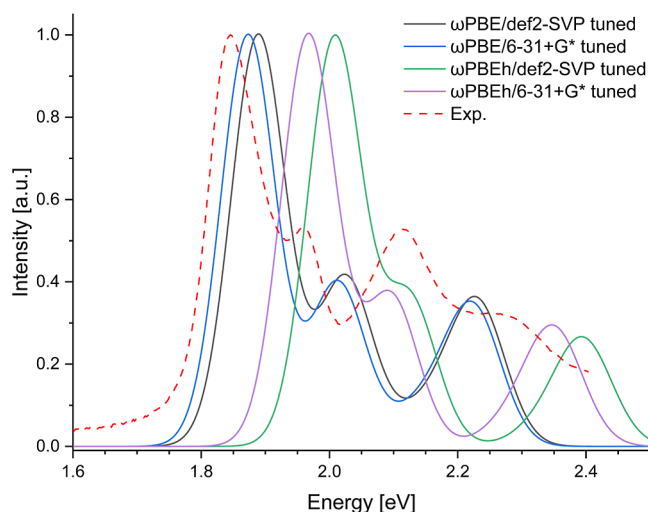
Tuning double hybrid functionals proved to be challenging as different tuning approaches led to different optimal  $\omega$  values.<sup>4</sup> These difficulties might result since the calculation of ionization potentials involves perturbation corrections for the energies of the  $N - 1$ ,  $N$ , and  $N + 1$ -electron systems, while frontier orbital energies do not include these corrections. Thus, effectively different levels of theory are involved in the tuning procedure. A comprehensive discussion on this topic can be found in ref 91, in which it was assumed that  $\epsilon^{\text{RSX-DH}} \approx \epsilon^{\text{RSX}}$ . These results indicate the need for a more sophisticated tuning procedure when applying double hybrid functionals to organic semiconductors, which goes beyond the scope of this study.

The localization of the exciton on the distorted monomer is described by all tested functionals when the 1000 geometry is employed (Figure S14). The trends are the same as for the 0000 distortion, with the spectral shapes of  $\omega$ PBE,  $\omega$ PBEh, and  $\omega$ B97X-D3 being very similar. However, as mentioned above, this geometry does not lead to the correct absorption spectra.

For  $\omega$ PBE and  $\omega$ PBEh, the basis set influence was tested by comparing the spectra obtained with the def2-SVP and the 6-31+G\* basis sets (Figures 14 and S15).

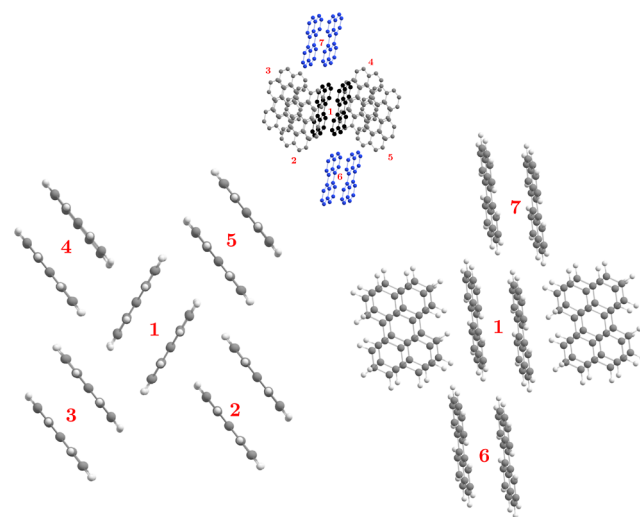
Def2-SVP-calculated spectra are slightly blue-shifted in comparison to those computed with 6-31+G\*. This effect is marginally larger for  $\omega$ PBEh (up to 0.05 eV) and therefore indicates that only small red shifts are expected if diffuse functions are added to the basis sets. The overall shape of the absorption spectra for both 0000 and 1000 is not influenced by the choice of basis set.

**3.6. Application to the Absorption Spectrum of  $\alpha$ -Perylene.** The aspects discussed so far for pentacene and tetracene show that cluster approaches seem to be able to simulate the absorption spectra of thin films or crystals adequately as long as the theoretical approach captures the energetic location of the CT states correctly. Additionally, the chosen cluster must reflect the symmetry of the crystal and allow for delocalization of the excitons over the entire cluster. The latter can only be achieved if all monomers of the cluster have as similar environments as possible. To investigate possible limitations of such cluster approaches, we focus on the absorption spectrum of the perylene crystal. Perylene is a well-studied prototypical material, as it is the parent molecule for a vast class of dyes. It crystallizes in monoclinic phases<sup>92</sup> called  $\alpha$ - and  $\beta$ -phases. The more complex  $\alpha$ -polymorph contains four molecules per unit cell arranged in a sandwich-



**Figure 14.** Comparison of total absorption spectra of the pentacene tetramer 1 cluster in the 0000 geometry (monomers optimized in a vacuum with  $\omega$ B97X-D3/def2-TZVP) computed with tuned  $\omega$ PBE and  $\omega$ PBEh using the def2-SVP and 6-31+G\* basis sets.

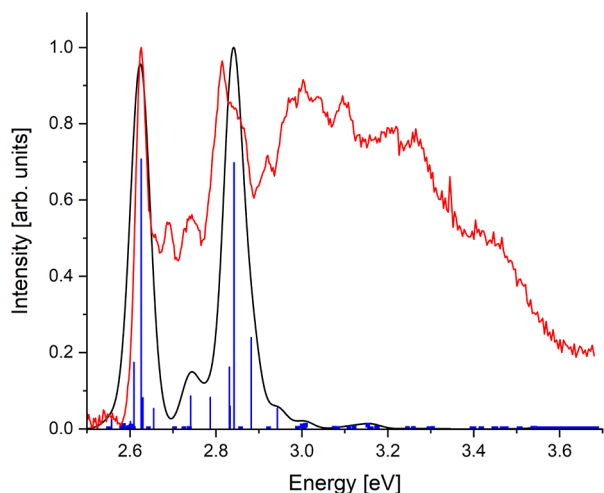
herringbone-like structure,<sup>93</sup> which is depicted in Figure 15 together with the clusters selected for computations. Each



**Figure 15.** Crystal structure excerpts used to investigate the absorption spectra of the monoclinic  $\alpha$ -phase of perylene. Upper part: sketch of the largest cluster, called 3D- $\alpha$ -Perylene. Left side: top view of the four molecules around the central dimer along a horizontal cut through the 3D- $\alpha$ -perylene cluster. The plane corresponds to the (b,c) crystal plane. Dimer 6 and 7 are omitted for clarity. The cluster containing dimers 1–5 is called 2D- $\alpha$ -perylene. Right-hand side: top view on the four molecules around the central dimer along a vertical cut through the 3D- $\alpha$ -perylene cluster. The dimers 2 and 4 are omitted for clarity. For the description of more clusters, see text and Figure S20.

dimer consists of two molecules aligned in parallel but slightly shifted with respect to each other. Therefore, we can explore possible limits of our approach using this structure, as it is impossible to cut out substructures in which all monomers have very similar environments. This raises the question of how a cluster of this nature must be composed (number and arrangement of monomers) to simulate the absorption spectra of the solids (crystals or thin films). In this respect, we first

focus on electronic effects since the corresponding clusters might be too large to include vibrational as well as relaxation effects. The experimental spectrum (Figure 16, red spectrum)



**Figure 16.** Absorption spectrum computed for the 3D- $\alpha$ -perylene cluster (black line) in comparison with the experimental spectrum (red line). The energetic positions of the electronic states are marked by the blue bars reflecting the calculated relative intensities. States with vanishing intensities are marked by squares. The experimental spectrum is blue-shifted by 0.21 eV.

is dominated by two peaks at about 2.6 and 2.8 eV. Between these peaks, the intensity decreases to some extent. The second dominant peak is followed by a broad absorption peak. Previous assignments attributed the two intense peaks to electronic excitations, while the region in between was mainly attributed to vibrational effects.<sup>26</sup> Such effects were also assigned to parts of the broad peak. Since we will focus on electronic effects, the vibrational progressions of bright electronic states are missing. Hence, the intensities computed with our approach are expected to be too low in comparison to the experimental data for parts of the spectrum where no bright electronically excited states are present.

The clusters used to simulate the spectrum are depicted in Figures 15 and S20. Beside the clusters named 2D- $\alpha$ -perylene and 3D- $\alpha$ -perylene, we also computed the spectrum for dimer 1 and a tetramer consisting of dimers 1 and 3 (Figure 15). Finally, we calculated the spectrum of an octamer (Figure S10). The latter was chosen since the environments of the dimers contained therein seem to be quite similar. As expected, neither dimer nor tetramer calculations can reliably simulate the experimental absorption spectrum (Figure S18 and Tables S28 and S29). But even the spectrum computed for the octamer (Figure S19 black line) differs considerably from the experimental one (Figure S19 red line) even when considering that vibrational effects have been neglected. The computed spectrum for the octamer cluster consists of three main peaks at about 2.9, 3.0, and 3.1 eV, i.e., the peaks are about 0.3 eV too high in energy compared to the experimental data. However, even more importantly than the energy shift, the computed intensity pattern does not agree with the measured one. This failure may result since the environments of the dimers are not as similar as they appear from Figure S20. As a consequence, localized as well as delocalized excitons are generated, as shown in Table S30. The state  $S_8$ , which is mainly responsible for the lowest computed band, is

delocalized, but  $S_{12}$  and  $S_{16}$ , which are responsible for bands 2 and 3, are mainly localized on dimer 4. The localization may arise since the couplings between the dimers are small and weak geometrical distortions already lead to a decoupling of the dimers. These small couplings between dimers may result because the coupling between both monomers within one dimer is very strong due to their planar mutual orientation. Most probably, the dimerization reduces the intermolecular interaction within a molecular layer relative to between molecules in different layers. Therefore, the restriction to a single molecular layer (as is the case for acene molecules) is no further justified. The exciton might be delocalized in three dimensions and not in two dimensions as is the case for acenes. The latter has been demonstrated for pentacene by Sharifzadeh.<sup>94</sup>

To test this, we enlarged the system to 2D- $\alpha$ -perylene and 3D- $\alpha$ -perylene (Figure 15). Employing the cluster 2D- $\alpha$ -perylene, which consists of five dimers reflecting another arrangement within one crystal plane, the computed spectrum agrees already qualitatively with the experimental one (Figure S18 and Table S31). The computed spectrum consists of two high peaks at 2.9 eV (10th excited state) and 3.2 eV (20th excited state), i.e. the two dominant peaks of the experimental spectrum are reproduced but are blue-shifted by about 0.4 eV with respect to their experimental energies. In addition, the calculated spectrum starts with a small shoulder at 2.7 eV (sixth excited state), which is missing in the experimental spectrum. When the cluster is extended by adding the two neighboring dimers of the central dimer above and below the crystal plane (Figure 15), the agreement between theory and experiment improves considerably. The shoulder at about 2.7 eV disappears and the energetic position of the two dominating peaks of the spectrum is only about 0.2 eV blue-shifted with respect to their experimental values. While the two dominating peaks are described well, the intensity between both dominating peaks is too low and the blue-shifted broad peak of the experimental spectrum is missing. For both ranges, the computations predict various electronic states, but the computed intensities nearly vanish. The significantly improved agreement of the spectrum obtained for 3D- $\alpha$ -perylene with the experiment proves that the coupling between dimers is so small that the exciton for  $\alpha$ -perylene is three-dimensionally delocalized. In contrast, for pentacenes and tetracene, the coupling between monomers in a plane appears to be so strong that two-dimensional excitons are generated upon absorption. Consequently, for  $\alpha$ -perylene on the one hand and tetracene and pentacene on the other hand, different dimensional clusters are necessary to reliably reproduce the thin-film absorption spectrum.

Before discussing reasons for the discrepancies between experiment and theory, we will assign the peaks in the spectrum to get more insights into why only the 3D- $\alpha$ -perylene cluster provides satisfactory agreement with the experiment. The characters of the involved electronic states can be taken from Table 6, which contains information about the five lowest states ( $S_1$ – $S_5$ ) together with those states with  $\mu_{i \rightarrow f} \geq 0.5$  D. The fragments for the e–h-correlation plots are the dimers indicated in Figure 15. A description of the remaining states up until 3.2 eV consisting of about 40 states can be found in Table S29. Information about even higher roots (in total we analyzed the lowest 100 states) are omitted, since they all show vanishing intensity. The studies of the hexamer cluster of pentacene showed that the lowest state was localized on the



Table 6. Characterization of the Most Important Lowest Lying Excited States of the 3D- $\alpha$ -Perylene Cluster<sup>a</sup>

$S_x$	E [eV]	$\mu_{i \rightarrow f}$ [D]	e-h-correlation plot	$S_x$	E [eV]	$\mu_{i \rightarrow f}$ [D]	e-h-correlation plot
1	2.762	0.004		20	2.953	3.214	
2	2.769	0.97		21	2.953	1.953	
3	2.793	0.087		22	2.999	3.027	
4	2.797	0.334		23	3.043	5.848	
5	2.800	0.034		24	3.045	2.155	
7	2.813	0.768		25	3.054	25.096	
10	2.821	6.782		26	3.054	2.218	
11	2.838	27.365		28	3.094	8.504	
12	2.842	3.176		30	3.155	1.901	
14	2.867	2.037					

<sup>a</sup>The table includes  $S_1$ – $S_5$  and states with  $\mu_{i \rightarrow f} \geq 0.5$  D.

inner pentacene monomer. The same is found for the 3D cluster of perylene. According to the e–h-plots, the  $S_1$  state is completely and  $S_2$  is mainly localized on the inner dimer (Table 6). However, the calculated intensities are  $\leq 0.01$ , so both states have no influence on the shape of the absorption spectrum. In contrast, the exciton of the dominant transition of the first peak ( $S_0 \rightarrow S_{11}$ ) is delocalized over dimers 5, 6, and 7. The exciton of the transition dominating the second peak ( $S_0 \rightarrow S_{25}$ ) is also distributed on dimers 6 and 7, with dimer 2 involved in this transition. This analysis confirms that the excitons in  $\alpha$ -perylene are three-dimensional. All other transitions for which nonvanishing transition dipole moments have been calculated are below about 3.0 eV. Their characters vary from states being localized on one dimer (e.g.,  $S_{20}$ – $S_{24}$ ) to

states which are delocalized over the whole cluster or parts of it (e.g.,  $S_{12}$ ,  $S_{14}$ ,  $S_{26}$ ,  $S_{28}$ ). Near-vanishing transition dipole moments are predicted for all excited states above 3.0 eV. According to the e–h-correlation plots, they can be described as CT states between given dimers.

While the computed spectrum accurately reproduces the dominating peaks of the experimental spectrum at about 2.6 and 2.8 eV, the intensity between both peaks as well as the broad absorption peak starting at about 2.9 eV are nearly missing. As indicated by previous investigations, parts of these missing features can be attributed to vibrational effects, which are neglected in the present computations. However, we cannot exclude that an enlargement of the cluster would lead to additional electronic states with nonvanishing intensities.

Test calculations with increased cluster sizes failed due to software and hardware limitations.

As shown in Figure S18, which displays the computed spectrum of 3D- $\alpha$ -perylene using the nontuned  $\omega$ B97X-D3 functional, the optimal tuning approach is again essential for an accurate description of the spectrum as found for pentacene and tetracene.

#### 4. CONCLUSIONS

In summary, the utilization of optimally tuned TD-DFT in conjunction with a cluster-based approach has proven highly effective in reproducing the thin-film absorption spectra of pentacene and tetracene in great detail, even yielding polarization-resolved results. For that purpose, it is imperative that the selected cluster adheres to the stringent selection rules established in this work, specifically by encompassing the entire unit cell, being rotationally symmetrical, and treating each monomer equally well. Any deviation from these criteria results in incomplete exciton delocalization, ultimately leading to a mismatch with experimental observations. While using the crystal structure is sufficient to reproduce the spectral shape, equally distorting the monomers within the cluster toward the  $S_1$  equilibrium structure of pentacene or tetracene significantly minimizes excitation energy errors to  $\leq 0.1$  eV. The application of optimal tuning to the cluster directly instead of onto monomers plays a pivotal role in the entire process, effectively preventing the CT states from being excessively high in energy. Additionally, the incorporation of vibrational effects is crucial, as their omission results in the absence of higher peaks in the case of pentacene and the second band in the case of tetracene.

For  $\alpha$ -perylene, excellent agreement with the first two prominent, low-lying peaks in the experimental spectrum is obtained when employing the three-dimensional cluster, denoted as 3D- $\alpha$ -perylene, comprising an inner dimer and its immediate neighbors. As expected, the lowest exciton localizes on the inner dimer, but its corresponding intensity vanishes. The dominant bands result from excitons being delocalized over the neighbors of the inner dimer. This indicates that for  $\alpha$ -perylene, the generated excitons exhibit a three-dimensional structure, whereas those formed in tetracene and pentacene remain two-dimensional within one layer of the crystal. This difference is likely due to weaker coupling between the dimers within  $\alpha$ -perylene in comparison to the monomers forming the pentacene or tetracene solid states. The remaining deviations between the computed and measured spectra of  $\alpha$ -perylene are likely attributed to our initial focus on electronic effects, with the neglect of vibrational effects as a primary contributing factor.

Our investigations underscore the suitability of cluster-based approaches for simulating total and polarization-resolved absorption spectra, provided that the energetic positions of the CT states are accurately described and that the chosen clusters reflect the shapes of the generated excitons. Our novel cluster approach, accompanied by the devised selection rules for appropriately sized clusters, exemplifies how a judicious blend of chemical intuition can substantially reduce computational costs while yielding chemically meaningful and nearly quantitative results.

#### ■ ASSOCIATED CONTENT

##### SI Supporting Information

The Supporting Information is available free of charge at <https://pubs.acs.org/doi/10.1021/acs.jctc.3c01107>.

Overview of previous studies on OSC thin films, more details on selected monomer calculations and geometries, excited states' characterization, spectra of all clusters mentioned, and Cartesian coordinates of all structures (PDF)

#### ■ AUTHOR INFORMATION

##### Corresponding Author

Bernd Engels – Institut für Physikalische und Theoretische Chemie, Julius-Maximilians-Universität Würzburg, 97074 Würzburg, Germany; [orcid.org/0000-0003-3057-389X](https://orcid.org/0000-0003-3057-389X); Email: [bernd.engels@uni-wuerzburg.de](mailto:bernd.engels@uni-wuerzburg.de)

##### Authors

Luca Craciunescu – Institut für Physikalische und Theoretische Chemie, Julius-Maximilians-Universität Würzburg, 97074 Würzburg, Germany; Institute of Chemical Sciences, School of Engineering and Physical Sciences, Heriot-Watt University, Edinburgh EH14 4AS Scotland, U.K.; [orcid.org/0000-0001-6468-2467](https://orcid.org/0000-0001-6468-2467)

Maximilian Asbach – Institut für Physikalische und Theoretische Chemie, Julius-Maximilians-Universität Würzburg, 97074 Würzburg, Germany

Sara Wirsing – Institut für Physikalische und Theoretische Chemie, Julius-Maximilians-Universität Würzburg, 97074 Würzburg, Germany; [orcid.org/0000-0002-8715-9959](https://orcid.org/0000-0002-8715-9959)

Sebastian Hammer – Experimentelle Physik VI, Julius-Maximilians-Universität Würzburg, Am Hubland 97074 Würzburg, Germany; Center for the Physics of Materials, Department of Physics and Department of Chemistry, McGill University, Montreal H3A 2K6 Québec, Canada; [orcid.org/0000-0002-0458-4133](https://orcid.org/0000-0002-0458-4133)

Frederik Unger – Institut für Angewandte Physik, Universität Tübingen, 72076 Tübingen, Germany; [orcid.org/0000-0002-7127-3829](https://orcid.org/0000-0002-7127-3829)

Katharina Broch – Institut für Angewandte Physik, Universität Tübingen, 72076 Tübingen, Germany; [orcid.org/0000-0002-9354-292X](https://orcid.org/0000-0002-9354-292X)

Frank Schreiber – Institut für Angewandte Physik, Universität Tübingen, 72076 Tübingen, Germany; [orcid.org/0000-0003-3659-6718](https://orcid.org/0000-0003-3659-6718)

Gregor Witte – Molekulare Festkörperphysik, Philipps-Universität Marburg, 35032 Marburg, Germany; [orcid.org/0000-0003-2237-0953](https://orcid.org/0000-0003-2237-0953)

Andreas Dreuw – Interdisziplinäres Zentrum für Wissenschaftliches Rechnen, Universität Heidelberg, 69120 Heidelberg, Germany; [orcid.org/0000-0002-5862-5113](https://orcid.org/0000-0002-5862-5113)

Petra Tegeder – Physikalisch-Chemisches Institut, Universität Heidelberg, 69120 Heidelberg, Germany; [orcid.org/0000-0002-5071-9385](https://orcid.org/0000-0002-5071-9385)

Felipe Fantuzzi – School of Chemistry and Forensic Science, University of Kent, CT2 7NH Canterbury, U.K.; [orcid.org/0000-0002-8200-8262](https://orcid.org/0000-0002-8200-8262)

Complete contact information is available at: <https://pubs.acs.org/doi/10.1021/acs.jctc.3c01107>

##### Notes

The authors declare no competing financial interest.

#### ■ ACKNOWLEDGMENTS

L.C. and M.A. carried out the calculations for the tetracene/pentacene and perylene, respectively, and prepared the

computed data for interpretation. All authors jointly interpreted the data, established important links to the experiments, and wrote the paper. The authors thank Jens Pflaum, Stephan Kümmel, and Leeor Kronik for fruitful discussions. S.H. acknowledges funding by the German Research Foundation (DFG) through the project 490894053. P.T. acknowledges funding by the DFG through the project TE479/6-1. F.U., K.B., and F.S. acknowledge funding by the DFG (BR4869/4-1 and SCHR700/40-1). The authors gratefully acknowledge the computing time provided to them on the high-performance computer Noctua2 at the NHR Center PC2. This system is funded by the Federal Ministry of Education and Research and the state governments participating on the basis of the resolutions of the GWK for national high-performance computing at universities ([www.nhr-verein.de/unsere-partner](http://www.nhr-verein.de/unsere-partner), accessed on Oct 06, 2023). The authors gratefully acknowledge the computational and data resources provided by the Leibniz Supercomputing Centre ([www.lrz.de](http://www.lrz.de), accessed on Oct 06, 2023).

## ■ ADDITIONAL NOTE

<sup>a</sup>Using the LUMO of the neutral system or the SOMO of the anion in the tuning procedure results in opposite trends for the optimal  $\omega$  when using SCF or DH energies for  $\omega$ B2PLYP. For RSX-QIDH, the trends reverse in an opposite fashion when using different frontier orbitals within one set of energies (DH or SCF).

## ■ REFERENCES

- (1) Spano, F. C. The Spectral Signatures of Frenkel Polarons in H- and J-Aggregates. *Acc. Chem. Res.* **2010**, *43*, 429–439.
- (2) Schröter, M.; Ivanov, S.; Schulze, J.; Polyutov, S.; Yan, Y.; Pullerits, T.; Kühn, O. Exciton–vibrational coupling in the dynamics and spectroscopy of Frenkel excitons in molecular aggregates. *Phys. Rep.* **2015**, *567*, 1–78.
- (3) Yamagata, H.; Norton, J.; Hontz, E.; Olivier, Y.; Beljonne, D.; Brédas, J. L.; Silbey, R. J.; Spano, F. C. The nature of singlet excitons in oligoacene molecular crystals. *J. Chem. Phys.* **2011**, *134*, 204703.
- (4) Berkelbach, T. C.; Hybertsen, M. S.; Reichman, D. R. Microscopic theory of singlet exciton fission. III. Crystalline pentacene. *J. Chem. Phys.* **2014**, *141*, 074705.
- (5) Beljonne, D.; Yamagata, H.; Brédas, J. L.; Spano, F. C.; Olivier, Y. Charge-Transfer Excitations Steer the Davydov Splitting and Mediate Singlet Exciton Fission in Pentacene. *Phys. Rev. Lett.* **2013**, *110*, 226402.
- (6) Bialas, A. L.; Spano, F. C. A Holstein–Peierls Approach to Excimer Spectra: The Evolution from Vibronically Structured to Unstructured Emission. *J. Phys. Chem. C* **2022**, *126*, 4067–4081.
- (7) Tiago, M. L.; Northrup, J. E.; Louie, S. G. Ab initio calculation of the electronic and optical properties of solid pentacene. *Phys. Rev. B: Condens. Matter Mater. Phys.* **2003**, *67*, 115212.
- (8) Cudazzo, P.; Gatti, M.; Rubio, A. Excitons in molecular crystals from first-principles many-body perturbation theory: Picene versus pentacene. *Phys. Rev. B: Condens. Matter Mater. Phys.* **2012**, *86*, 195307.
- (9) Cocchi, C.; Breuer, T.; Witte, G.; Draxl, C. Polarized absorbance and Davydov splitting in bulk and thin-film pentacene polymorphs. *Phys. Chem. Chem. Phys.* **2018**, *20*, 29724–29736.
- (10) Leng, X.; Feng, J.; Chen, T.; Liu, C.; Ma, Y. Optical properties of acene molecules and pentacene crystal from the many-body Green's function method. *Phys. Chem. Chem. Phys.* **2016**, *18*, 30777–30784.
- (11) Cocchi, C.; Guerrini, M.; Krumland, J.; Trung Nguyen, N.; Valencia, A. M. Modeling the electronic structure of organic materials: a solid-state physicist's perspective. *J. Phys.: Mater.* **2022**, *6*, 012001.
- (12) Valencia, A. M.; Bischof, D.; Anhäuser, S.; Zeplichal, M.; Terfort, A.; Witte, G.; Cocchi, C. Excitons in organic materials: revisiting old concepts with new insights. *Electron. Struct.* **2023**, *5*, 033003.
- (13) Engels, B.; Engel, V. The dimer-approach to characterize optoelectronic properties of and exciton trapping and diffusion in organic semiconductor aggregates and crystals. *Phys. Chem. Chem. Phys.* **2017**, *19*, 12604–12619.
- (14) Wirsing, S.; Hänsel, M.; Belova, V.; Schreiber, F.; Broch, K.; Engels, B.; Tegeder, P. Excited-State Dynamics in Perylene-Based Organic Semiconductor Thin Films: Theory Meets Experiment. *J. Phys. Chem. C* **2019**, *123*, 27561–27572.
- (15) Bellingier, D.; Pflaum, J.; Brüning, C.; Engel, V.; Engels, B. The electronic character of PTCDA thin films in comparison to other perylene-based organic semi-conductors: ab initio-TD-DFT and semi-empirical computations of the opto-electronic properties of large aggregates. *Phys. Chem. Chem. Phys.* **2017**, *19*, 2434–2448.
- (16) Brückner, C.; Würthner, F.; Meerholz, K.; Engels, B. Structure–Property Relationships from Atomistic Multiscale Simulations of the Relevant Processes in Organic Solar Cells. I. Thermodynamic Aspects. *J. Phys. Chem. C* **2017**, *121*, 4–25.
- (17) Brückner, C.; Würthner, F.; Meerholz, K.; Engels, B. Atomistic Approach To Simulate Processes Relevant for the Efficiencies of Organic Solar Cells as a Function of Molecular Properties. II. Kinetic Aspects. *J. Phys. Chem. C* **2017**, *121*, 26–51.
- (18) Hammer, S.; Zeiser, C.; Deutsch, M.; Engels, B.; Broch, K.; Pflaum, J. Spatial Anisotropy of Charge Transfer at Perfluoropentacene–Pentacene (001) Single-Crystal Interfaces and its Relevance for Thin Film Devices. *ACS Appl. Mater. Interfaces* **2020**, *12*, 53547–53556.
- (19) Müller, U.; Roos, L.; Frank, M.; Deutsch, M.; Hammer, S.; Krumrein, M.; Friedrich, A.; Marder, T. B.; Engels, B.; Krueger, A.; Pflaum, J. Role of Intermolecular Interactions in the Excited-State Photophysics of Tetracene and 2,2'-Ditetracene. *J. Phys. Chem. C* **2020**, *124*, 19435–19446.
- (20) Craciunescu, L.; Wirsing, S.; Hammer, S.; Broch, K.; Dreuw, A.; Fantuzzi, F.; Sivanesan, V.; Tegeder, P.; Engels, B. Accurate Polarization-Resolved Absorption Spectra of Organic Semiconductor Thin Films Using First-Principles Quantum-Chemical Methods: Pentacene as a Case Study. *J. Phys. Chem. Lett.* **2022**, *13*, 3726–3731.
- (21) Stein, T.; Kronik, L.; Baer, R. Reliable Prediction of Charge Transfer Excitations in Molecular Complexes Using Time-Dependent Density Functional Theory. *J. Am. Chem. Soc.* **2009**, *131*, 2818–2820.
- (22) Alam, B.; Morrison, A. F.; Herbert, J. M. Charge Separation and Charge Transfer in the Low-Lying Excited States of Pentacene. *J. Phys. Chem. C* **2020**, *124*, 24653–24666.
- (23) Sebastian, L.; Weiser, G.; Bässler, H. Charge transfer transitions in solid tetracene and pentacene studied by electroabsorption. *Chem. Phys.* **1981**, *61*, 125–135.
- (24) Zeiser, C.; Moretti, L.; Lepple, D.; Cerullo, G.; Maiuri, M.; Broch, K. Singlet Heterofission in Tetracene–Pentacene Thin-Film Blends. *Angew. Chem., Int. Ed.* **2020**, *59*, 19966–19973.
- (25) Bree, A.; Lyons, L. E. 1002. The intensity of ultraviolet-light absorption by monocrystals. Part IV. Absorption by naphthacene of plane-polarized light. *J. Chem. Soc.* **1960**, S206–S212.
- (26) Rangel, T.; Rinn, A.; Sharifzadeh, S.; da Jornada, F. H.; Pick, A.; Louie, S. G.; Witte, G.; Kronik, L.; Neaton, J. B.; Chatterjee, S. Low-lying excited states in crystalline perylene. *Proc. Natl. Acad. Sci. U.S.A.* **2018**, *115*, 284–289.
- (27) Hinderhofer, A.; Heinemeyer, U.; Gerlach, A.; Kowarik, S.; Jacobs, R. M. J.; Sakamoto, Y.; Suzuki, T.; Schreiber, F. Optical properties of pentacene and perfluoropentacene thin films. *J. Chem. Phys.* **2007**, *127*, 194705.
- (28) Perić, M.; Engels, B.; Peyerimhoff, S. D. Ab initio investigation of the vibronic structure of the C2H spectrum: Calculation of the hyperfine coupling constants for the three lowest-lying electronic states. *J. Mol. Spectrosc.* **1991**, *150*, 56–69.
- (29) Perić, M.; Engels, B.; Peyerimhoff, S. D. Ab initio investigation of the vibronic structure of the C2H spectrum: Computation of the



- vibronically averaged values for the hyperfine coupling constants. *J. Mol. Spectrosc.* **1991**, *150*, 70–85.
- (30) Silva-Junior, M. R.; Schreiber, M.; Sauer, S. P. A.; Thiel, W. Benchmarks for electronically excited states: Basis set effects on CASPT2 results. *J. Chem. Phys.* **2010**, *133*, 174318.
- (31) Silva-Junior, M. R.; Schreiber, M.; Sauer, S. P. A.; Thiel, W. Benchmarks for electronically excited states: Time-dependent density functional theory and density functional theory based multireference configuration interaction. *J. Chem. Phys.* **2008**, *129*, 104103.
- (32) Schmittel, M.; Steffen, J.-P.; Maywald, M.; Engels, B.; Helten, H.; Musch, P. Ring size effects in the C2–C6 biradical cyclisation of enyne–allenes and the relevance for neocarzinostatin. *J. Chem. Soc., Perkin Trans. 2* **2001**, *2*, 1331–1339.
- (33) Pless, V.; Suter, H. U.; Engels, B. Ab initio study of the energy difference between the cyclic and linear forms of the C6 molecule. *J. Chem. Phys.* **1994**, *101*, 4042–4048.
- (34) Suter, H.; Pleß, V.; Ernzerhof, M.; Engels, B. Difficulties in the calculation of electron spin resonance parameters using density functional methods. *Chem. Phys. Lett.* **1994**, *230*, 398–404.
- (35) Engels, B. Study of influences of various excitation classes on ab initio calculated isotropic hyperfine coupling constants. *Theor. Chim. Acta* **1993**, *86*, 429–437.
- (36) Engels, B. A detailed study of the configuration selected multireference configuration interaction method combined with perturbation theory to correct the wave function. *J. Chem. Phys.* **1994**, *100*, 1380–1386.
- (37) Christiansen, O.; Koch, H.; Jørgensen, P. The second-order approximate coupled cluster singles and doubles model CC2. *Chem. Phys. Lett.* **1995**, *243*, 409–418.
- (38) Grimme, S. Improved second-order Møller–Plesset perturbation theory by separate scaling of parallel- and antiparallel-spin pair correlation energies. *J. Chem. Phys.* **2003**, *118*, 9095–9102.
- (39) Hellweg, A.; Grün, S. A.; Hättig, C. Benchmarking the performance of spin-component scaled CC2 in ground and electronically excited states. *Phys. Chem. Chem. Phys.* **2008**, *10*, 4119–4127.
- (40) Nooijen, M.; Bartlett, R. J. A new method for excited states: Similarity transformed equation-of-motion coupled-cluster theory. *J. Chem. Phys.* **1997**, *106*, 6441–6448.
- (41) Riplinger, C.; Neese, F. An efficient and near linear scaling pair natural orbital based local coupled cluster method. *J. Chem. Phys.* **2013**, *138*, 034106.
- (42) Riplinger, C.; Sandhoefer, B.; Hansen, A.; Neese, F. Natural triple excitations in local coupled cluster calculations with pair natural orbitals. *J. Chem. Phys.* **2013**, *139*, 134101.
- (43) Neese, F. The ORCA program system. *Wiley Interdiscip. Rev.: Comput. Mol. Sci.* **2012**, *2*, 73–78.
- (44) Ekström, U.; Visscher, L.; Bast, R.; Thorvaldsen, A. J.; Ruud, K. Arbitrary-Order Density Functional Response Theory from Automatic Differentiation. *J. Chem. Theory Comput.* **2010**, *6*, 1971–1980.
- (45) Valeev, E. F. *Libint: A Library for the Evaluation of Molecular Integrals of Many-Body Operators over Gaussian Functions*, Version 2.7.0-beta.6, 2020. <http://libint.valeev.net/>.
- (46) Shao, Y.; Gan, Z.; Epifanovsky, E.; Gilbert, A. T.; Wormit, M.; Kussmann, J.; Lange, A. W.; Behn, A.; Deng, J.; Feng, X.; Ghosh, D.; Goldey, M.; Horn, P. R.; Jacobson, L. D.; Kaliman, I.; Khaliullin, R. Z.; Kus, T.; Landau, A.; Liu, J.; Proynov, E. I.; Rhee, Y. M.; Richard, R. M.; Rohrdanz, M. A.; Steele, R. P.; Sundstrom, E. J.; Woodcock, H. L., III; Zimmerman, P. M.; Zuev, D.; Albrecht, B.; Alguire, E.; Austin, B.; Beran, G. J. O.; Bernard, Y. A.; Berquist, E.; Brandhorst, K.; Bravaya, K. B.; Brown, S. T.; Casanova, D.; Chang, C.-M.; Chen, Y.; Chien, S. H.; Closser, K. D.; Crittenden, D. L.; Diedenhofen, M.; DiStasio, R. A., Jr.; Do, H.; Dutoi, A. D.; Edgar, R. G.; Fatehi, S.; Fusti-Molnar, L.; Ghysels, A.; Golubeva-Zadorozhnaya, A.; Gomes, J.; Hanson-Heine, M. W.; Harbach, P. H.; Hauser, A. W.; Hohenstein, E. G.; Holden, Z. C.; Jagau, T.-C.; Ji, H.; Kaduk, B.; Khistyayev, K.; Kim, J.; Kim, J.; King, R. A.; Klunzinger, P.; Kosenkov, D.; Kowalczyk, T.; Krauter, C. M.; Lao, K. U.; Laurent, A. D.; Lawler, K. V.; Levchenko, S. V.; Lin, C. Y.; Liu, F.; Livshits, E.; Lochan, R. C.; Luenser, A.; Manohar, P.; Manzer, S. F.; Mao, S.-P.; Mardirossian, N.; Marenich, A. V.; Maurer, S. A.; Mayhall, N. J.; Neuscamman, E.; Oana, C. M.; Olivares-Amaya, R.; O'Neill, D. P.; Parkhill, J. A.; Perrine, T. M.; Peverati, R.; Prociuk, A.; Rehn, D. R.; Rosta, E.; Russ, N. J.; Sharada, S. M.; Sharma, S.; Small, D. W.; Sodt, A.; Stein, T.; Stück, D.; Su, Y.-C.; Thom, A. J.; Tsuchimochi, T.; Vanovschi, V.; Vogt, L.; Vydrov, O.; Wang, T.; Watson, M. A.; Wenzel, J.; White, A.; Williams, C. F.; Yang, J.; Yeganeh, S.; Yost, S. R.; You, Z.-Q.; Zhang, I. Y.; Zhang, X.; Zhao, Y.; Brooks, B. R.; Chan, G. K.; Chipman, D. M.; Cramer, C. J.; Goddard, W. A., III; Gordon, M. S.; Hehre, W. J.; Klamt, A.; Schaefer, H. F., III; Schmidt, M. W.; Sherrill, C. D.; Truhlar, D. G.; Warshel, A.; Xu, X.; Aspuru-Guzik, A.; Baer, R.; Bell, A. T.; Besley, N. A.; Chai, J.-D.; Dreuw, A.; Dunietz, B. D.; Furlani, T. R.; Gwaltney, S. R.; Hsu, C.-P.; Jung, Y.; Kong, J.; Lambrecht, D. S.; Liang, W.; Ochsenfeld, C.; Rassolov, V. A.; Slipchenko, L. V.; Subotnik, J. E.; Van Voorhis, T.; Herbert, J. M.; Krylov, A. I.; Gill, P. M.; Head-Gordon, M. Advances in molecular quantum chemistry contained in the Q-Chem 4 program package. *Mol. Phys.* **2015**, *113*, 184–215.
- (47) Fdez Galván, I.; Vacher, M.; Alavi, A.; Angeli, C.; Aquilante, F.; Autschbach, J.; Bao, J. J.; Bokarev, S. I.; Bogdanov, N. A.; Carlson, R. K.; Chibotaru, L. F.; Creutzberg, J.; Dattani, N.; Delcey, M. G.; Dong, S. S.; Dreuw, A.; Freitag, L.; Frutos, L. M.; Gagliardi, L.; Gendron, F.; Giussani, A.; González, L.; Grell, G.; Guo, M.; Hoyer, C. E.; Johansson, M.; Keller, S.; Knecht, S.; Kovačević, G.; Källman, E.; Li Manni, G.; Lundberg, M.; Ma, Y.; Mai, S.; Malhado, J. P.; Malmqvist, P. A.; Marquetand, P.; Mewes, S. A.; Norell, J.; Olivucci, M.; Oppel, M.; Phung, Q. M.; Pierloot, K.; Plasser, F.; Reiher, M.; Sand, A. M.; Schapiro, I.; Sharma, P.; Stein, C. J.; Sørensen, L. K.; Truhlar, D. G.; Ugandi, M.; Ungur, L.; Valentini, A.; Vancollie, S.; Veryazov, V.; Weser, O.; Wesolowski, T. A.; Widmark, P.-O.; Wouters, S.; Zech, A.; Zobel, J. P.; Lindh, R. OpenMolcas: From Source Code to Insight. *J. Chem. Theory Comput.* **2019**, *15*, S925–S964.
- (48) Aquilante, F.; Autschbach, J.; Baiardi, A.; Battaglia, S.; Borin, V. A.; Chibotaru, L. F.; Conti, I.; De Vico, L.; Delcey, M.; Fdez Galván, I.; Ferré, N.; Freitag, L.; Garavelli, M.; Gong, X.; Knecht, S.; Larsson, E. D.; Lindh, R.; Lundberg, M.; Malmqvist, P. A.; Nenov, A.; Norell, J.; Odelius, M.; Olivucci, M.; Pedersen, T. B.; Pedraza-González, L.; Phung, Q. M.; Pierloot, K.; Reiher, M.; Schapiro, I.; Segarra-Martí, J.; Segatta, F.; Seijo, L.; Sen, S.; Sergentu, D.-C.; Stein, C. J.; Ungur, L.; Vacher, M.; Valentini, A.; Veryazov, V. Modern quantum chemistry with [Open]Molcas. *J. Chem. Phys.* **2020**, *152*, 214117.
- (49) Gonzalez, L. In *Quantum Chemistry and Dynamics of Excited States: Methods and Applications*; Gonzalez, L., Lindh, R., Eds.; Wiley-Blackwell: Hoboken, NJ, 2020.
- (50) Hättig, C.; Weigend, F. CC2 excitation energy calculations on large molecules using the resolution of the identity approximation. *J. Chem. Phys.* **2000**, *113*, 5154–5161.
- (51) Hättig, C. Structure Optimizations for Excited States with Correlated Second-Order Methods: CC2 and ADC(2). *Adv. Quantum Chem.* **2005**, *50*, 37–60.
- (52) TURBOMOLE V7.4 2019, a Development of University of Karlsruhe and Forschungszentrum Karlsruhe GmbH, 1989–2007; TURBOMOLE GmbH, since 2007; available from <http://www.turbomole.com>.
- (53) Plasser, F. TheoDORE A toolbox for a detailed and automated analysis of electronic excited state computations. *J. Chem. Phys.* **2020**, *152*, 084108.
- (54) Dreuw, A.; Weisman, J. L.; Head-Gordon, M. Long-range charge-transfer excited states in time-dependent density functional theory require non-local exchange. *J. Chem. Phys.* **2003**, *119*, 2943–2946.
- (55) Fink, R. F.; Pfister, J.; Zhao, H. M.; Engels, B. Assessment of quantum chemical methods and basis sets for excitation energy transfer. *Chem. Phys.* **2008**, *346*, 275–285.
- (56) Settels, V.; Schubert, A.; Tafipolski, M.; Liu, W.; Stehr, V.; Topczak, A. K.; Pflaum, J.; Deibel, C.; Fink, R. F.; Engel, V.; Engels, B. Identification of Ultrafast Relaxation Processes As a Major Reason for Inefficient Exciton Diffusion in Perylene-Based Organic Semiconductors. *J. Am. Chem. Soc.* **2014**, *136*, 9327–9337.

- (57) Iikura, H.; Tsuneda, T.; Yanai, T.; Hirao, K. A long-range correction scheme for generalized-gradient-approximation exchange functionals. *J. Chem. Phys.* **2001**, *115*, 3540–3544.
- (58) Leininger, T.; Stoll, H.; Werner, H.-J.; Savin, A. Combining long-range configuration interaction with short-range density functionals. *Chem. Phys. Lett.* **1997**, *275*, 151–160.
- (59) Peach, M. J. G.; Benfield, P.; Helgaker, T.; Tozer, D. J. Excitation energies in density functional theory: An evaluation and a diagnostic test. *J. Chem. Phys.* **2008**, *128*, 044118.
- (60) Stein, T.; Eisenberg, H.; Kronik, L.; Baer, R. Fundamental Gaps in Finite Systems from Eigenvalues of a Generalized Kohn-Sham Method. *Phys. Rev. Lett.* **2010**, *105*, 266802.
- (61) Kronik, L.; Stein, T.; Refaely-Abramson, S.; Baer, R. Excitation Gaps of Finite-Sized Systems from Optimally Tuned Range-Separated Hybrid Functionals. *J. Chem. Theory Comput.* **2012**, *8*, 1515–1531.
- (62) Almbladh, C. O.; von Barth, U. Exact results for the charge and spin densities, exchange-correlation potentials, and density-functional eigenvalues. *Phys. Rev. B: Condens. Matter Mater. Phys.* **1985**, *31*, 3231–3244.
- (63) Refaely-Abramson, S.; Sharifzadeh, S.; Jain, M.; Baer, R.; Neaton, J. B.; Kronik, L. Gap renormalization of molecular crystals from density-functional theory. *Phys. Rev. B: Condens. Matter Mater. Phys.* **2013**, *88*, 081204.
- (64) Tamblyn, I.; Refaely-Abramson, S.; Neaton, J. B.; Kronik, L. Simultaneous Determination of Structures, Vibrations, and Frontier Orbital Energies from a Self-Consistent Range-Separated Hybrid Functional. *J. Phys. Chem. Lett.* **2014**, *5*, 2734–2741.
- (65) Barone, V.; Cossi, M. Quantum Calculation of Molecular Energies and Energy Gradients in Solution by a Conductor Solvent Model. *J. Phys. Chem. A* **1998**, *102*, 1995–2001.
- (66) Kronik, L.; Kümmel, S. Dielectric Screening Meets Optimally Tuned Density Functionals. *Adv. Mater.* **2018**, *30*, 1706560.
- (67) Schiefer, S.; Huth, M.; Dobrinski, A.; Nickel, B. Determination of the Crystal Structure of Substrate-Induced Pentacene Polymorphs in Fiber Structured Thin Films. *J. Am. Chem. Soc.* **2007**, *129*, 10316–10317.
- (68) Campbell, R. B.; Robertson, J. M.; Trotter, J. The crystal structure of hexacene, and a revision of the crystallographic data for tetracene. *Acta Crystallogr.* **1962**, *15*, 289–290.
- (69) Biermann, D.; Schmidt, W. Diels-Alder reactivity of polycyclic aromatic hydrocarbons. 1. Acenes and benzologs. *J. Am. Chem. Soc.* **1980**, *102*, 3163–3173.
- (70) Coto, P. B.; Sharifzadeh, S.; Neaton, J. B.; Thoss, M. Low-Lying Electronic Excited States of Pentacene Oligomers: A Comparative Electronic Structure Study in the Context of Singlet Fission. *J. Chem. Theory Comput.* **2015**, *11*, 147–156.
- (71) Marian, C. M.; Gilka, N. Performance of the Density Functional Theory/Multireference Configuration Interaction Method on Electronic Excitation of Extended  $\pi$ -Systems. *J. Chem. Theory Comput.* **2008**, *4*, 1501–1515.
- (72) Halasinski, T. M.; Hudgins, D. M.; Salama, F.; Allamandola, L. J.; Bally, T. Electronic Absorption Spectra of Neutral Pentacene (C<sub>22</sub>H<sub>14</sub>) and Its Positive and Negative Ions in Ne, Ar, and Kr Matrices. *J. Phys. Chem. A* **2000**, *104*, 7484–7491.
- (73) Heinecke, E.; Hartmann, D.; Müller, R.; Hese, A. Laser spectroscopy of free pentacene molecules (I): The rotational structure of the vibrationless S<sub>1</sub> ← S<sub>0</sub> transition. *J. Chem. Phys.* **1998**, *109*, 906–911.
- (74) Jacquemin, D. What is the Key for Accurate Absorption and Emission Calculations, Energy or Geometry? *J. Chem. Theory Comput.* **2018**, *14*, 1534–1543.
- (75) Grimme, S.; Parac, M. Substantial Errors from Time-Dependent Density Functional Theory for the Calculation of Excited States of Large  $\pi$  Systems. *ChemPhysChem* **2003**, *4*, 292–295.
- (76) Winter, N. O. C.; Graf, N. K.; Leutwyler, S.; Hättig, C. Benchmarks for 0–0 transitions of aromatic organic molecules: DFT/B3LYP, ADC(2), CC2, SOS-CC2 and SCS-CC2 compared to high-resolution gas-phase data. *Phys. Chem. Chem. Phys.* **2013**, *15*, 6623–6630.
- (77) Gozem, S.; Krylov, A. I. The ezSpectra suite: An easy-to-use toolkit for spectroscopy modeling. *Wiley Interdiscip. Rev.: Comput. Mol. Sci.* **2022**, *12*, No. e1546.
- (78) Loos, P.-F.; Boggio-Pasqua, M.; Scemama, A.; Caffarel, M.; Jacquemin, D. Reference Energies for Double Excitations. *J. Chem. Theory Comput.* **2019**, *15*, 1939–1956.
- (79) Hait, D.; Head-Gordon, M. Orbital Optimized Density Functional Theory for Electronic Excited States. *J. Phys. Chem. Lett.* **2021**, *12*, 4517–4529.
- (80) Brillante, A.; Bilotti, I.; Della Valle, R.; Venuti, E.; Masino, M.; Girlando, A. Characterization of Phase Purity in Organic Semiconductors by Lattice-Phonon Confocal Raman Mapping: Application to Pentacene. *Adv. Mater.* **2005**, *17*, 2549–2553.
- (81) Girlando, A.; Grisanti, L.; Masino, M.; Brillante, A.; Della Valle, R. G.; Venuti, E. Interaction of charge carriers with lattice and molecular phonons in crystalline pentacene. *J. Chem. Phys.* **2011**, *135*, 084701.
- (82) Breuer, T.; Celik, M. A.; Jakob, P.; Tonner, R.; Witte, G. Vibrational Davydov Splittings and Collective Mode Polarizations in Oriented Organic Semiconductor Crystals. *J. Phys. Chem. C* **2012**, *116*, 14491–14503.
- (83) Faltermeier, D.; Gompf, B.; Dressel, M.; Tripathi, A. K.; Pflaum, J. Optical properties of pentacene thin films and single crystals. *Phys. Rev. B: Condens. Matter Mater. Phys.* **2006**, *74*, 125416.
- (84) Helzel, J.; Jankowski, S.; El Helou, M.; Witte, G.; Heimbrodt, W. Temperature dependent optical properties of pentacene films on zinc oxide. *Appl. Phys. Lett.* **2011**, *99*, 211102.
- (85) El Helou, M.; Lietke, E.; Helzel, J.; Heimbrodt, W.; Witte, G. Structural and optical properties of pentacene films grown on differently oriented ZnO surfaces. *J. Phys.: Condens. Matter* **2012**, *24*, 445012.
- (86) Shirovani, I.; Kamura, Y.; Inokuchi, H. Effect of Pressure on the Absorption Spectra of Oriented and Amorphous Organic Films. *Mol. Cryst. Liq. Cryst.* **1974**, *28*, 345–353.
- (87) Hammer, S. T. Influence of Crystal Structure on Excited States in Crystalline Organic Semiconductors. Ph.D. Thesis, Universität Würzburg, 2021.
- (88) Dressel, M.; Gompf, B.; Faltermeier, D.; Tripathi, A.; Pflaum, J.; Schubert, M. Kramers-Kronig-consistent optical functions of anisotropic crystals: generalized spectroscopic ellipsometry on pentacene. *Opt. Express* **2008**, *16*, 19770–19778.
- (89) Brémond, É.; Savarese, M.; Pérez-Jiménez, Á. J.; Sancho-García, J. C.; Adamo, C. Range-Separated Double-Hybrid Functional from Nonempirical Constraints. *J. Chem. Theory Comput.* **2018**, *14*, 4052–4062.
- (90) Casanova-Páez, M.; Dardis, M. B.; Goerigk, L.  $\omega$ B2PLYP and  $\omega$ B2GPPLYP: The First Two Double-Hybrid Density Functionals with Long-Range Correction Optimized for Excitation Energies. *J. Chem. Theory Comput.* **2019**, *15*, 4735–4744.
- (91) Brémond, É.; Pérez-Jiménez, Á. J.; Sancho-García, J. C.; Adamo, C. Range-separated hybrid and double-hybrid density functionals: A quest for the determination of the range-separation parameter. *J. Chem. Phys.* **2020**, *152*, 244124.
- (92) Tanaka, J. The Electronic Spectra of Aromatic Molecular Crystals. II. The Crystal Structure and Spectra of Perylene. *Bull. Chem. Soc. Jpn.* **1963**, *36*, 1237–1249.
- (93) Botoshansky, M.; Herstein, F. H.; Kapon, M. Towards a complete description of a polymorphic crystal: The example of perylene: Redetermination of the structures of the (Z= 2 and 4) polymorphs. *Helv. Chim. Acta* **2003**, *86*, 1113–1128.
- (94) Sharifzadeh, S.; Darancet, P.; Kronik, L.; Neaton, J. B. Low-Energy Charge-Transfer Excitons in Organic Solids from First-Principles: The Case of Pentacene. *J. Phys. Chem. Lett.* **2013**, *4*, 2197–2201.